International Journal of Biological Macromolecules 253 (2023) 126618

Contents lists available at ScienceDirect

International Journal of Biological Macromolecules

journal homepage: www.elsevier.com/locate/ijbiomac

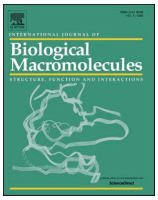

In-vitro and in-vivo evaluation for the bio-natural Alginate/nano-Hydroxyapatite (Alg/n-HA) injectable hydrogel for critical size bone substitution

Abeer M. El-Kady [a], E.M. Mahmoud [b,*], M. Sayed [b], S.M. Kamel [c], S.M. Naga [b]

[a] Glass Research Department, National Research Centre, El-Bohous Str., 12622 Cairo, Egypt
[b] Ceramics Department, National Research Centre, El-Bohous Str., 12622 Cairo, Egypt
[c] Oral Biology Department, MSA University, Egypt

ARTICLE INFO

Keywords:
Injectable hydrogel
Bone treatment
Alginate
Viscosity
In-vitro
In-vivo

ABSTRACT

Currently, bio-natural injectable hydrogels are receiving a lot of attention due to their ability to control, adjust, and adapt to random bone defects, in addition, to their ability to mimic the composition of natural bones. From such a viewpoint, this study goal is to prepare and characterize the injectable hydrogels paste based on the natural alginate (Alg) derived from brown sea algae as a polysaccharide polymer, which coupled with nano biogenic-hydroxyapatite (n-HA) prepared from eggshells and enriched with valuable trace elements. The viscosity and mechanical properties of the paste were investigated. As well as the in-vitro study in terms of water absorption and biodegradability in the PBS, biocompatibility and the capability of the injectable Alginate/n-Hydroxyapatite (Alg/n-HA) to regenerate bone for the most suitable injectable form. The injectable hydrogel (BP -B sample) was chosen for the study as it had an appropriate setting time for injecting (13 mins), and suitable compressive strength reached 6.3 MPa. The in vivo study was also carried out including a post-surgery follow-up test of the newly formed bone (NB) in the defect area after 10 and 20 weeks using different techniques such as (SEM/EDX) and histological analysis, the density of the newly formed bone by Dual x-ray absorptiometry (DEXA), blood biochemistry and the radiology test. The results proved that the injectable hydrogels Alginate/n-Hydroxyapatite (Alg/n-HA) had an appreciated biodegradability and bioactivity, which allow the progress of angiogenesis, endochondral ossification, and osteogenesis throughout the defect area, which positively impacts the healing time and ensures the full restoration for the well-mature bone tissue that similar to the natural bone.

1. Introduction

Invasive reconstruction surgery using fixed-shaped synthetic implants for defective bone treatment has shown some severe complications, especially in cases of irregular, asymmetrical or twisted shape defects induced by trauma or massive tumor resection [1]. This is because it's impossible for surgeons to fit the implant into that random space. Hence, the outline of the defect margin must be adjusted to match the inserted implant, which creates a larger defect area. This adjusting process necessitates a prolonged healing stage, higher morbid rate and intolerable pain for the patient. In contrast, injectable natural or synthetic polymers can be easily introduced into the defect area through a small insertion by a syringe. The most important benefit gained using this injectable technique includes; the creation of a smaller wound site combined with a superior healing stage and endurable pain for the patient [2–6]. Injectable polymeric materials can simply diffuse, fill and

Abbreviations: PBS, Phosphate buffer solution; BMD, Bone mineral density; Hb, Hemoglobin level; PLT, Platelets count; ALP, Alkaline phosphatase; AST, Aspartate aminotransferase; ALT, Alanine aminotransferase; LIP, Lipid hydroperoxide levels; GSH, Glutathione reductase level; SOD, Superoxide dismutase; NO, Nitric oxide; ARG, Arginase; AFU, α-L-Fucosidase; RBC, Erythrocyte; WBCs, Leucocyte count; SD, Standard deviation; SIG (ρ), Significant value; ICP, Inductively coupled plasma; TEM, Transmission electron microscopy; SEM, Scanning electron microscope; EDXs, Elemental dispersive X-ray; DEXA, Dual x-ray absorptiometry; XRF, X-ray fluorescence spectroscopy; FTIR, Fourier transform Infrared Spectrometer; UV, Ultraviolet light; SBF, Simulated body fluids; BP-A, Injectable hydrogel -A; BP-B, Injectable hydrogel —B; BP-C, Injectable hydrogel —C; Alg, Sodium alginate; n-HA, Nano-hydroxyapatite; HOS, Bone osteosarcoma cell line; DMEM, Dulbecco's modified Eagle's medium; AP, Anteroposterior views; NB, Newly formed bone; IACUC, International Animal Care and Use Committee.

* Corresponding author.
E-mail address: dr_eman2006@yahoo.com (E.M. Mahmoud).

https://doi.org/10.1016/j.ijbiomac.2023.126618
Received 1 May 2023; Received in revised form 27 August 2023; Accepted 28 August 2023
Available online 1 September 2023

adapt to the randomly shaped defect. Once they settled inside the irregular space, they absorb water and swell forming a solidified gel with a well-organized and interconnected porous frame.

Injectable hydrogels are prepared using different techniques including; ionic interaction, thermal gelation, photo-polymerization, and chemical, and physical self-assembly [4,5,7]. Recently various types of natural or synthetic polymers based injectable and in situ-forming self-setting hydrogels were used extensively in the biomedical field as bone tissue engineering scaffolds and/or drug delivery systems [8–15]. Hydrogels created from natural polymers are more biocompatible and have superior biological behaviour over those originating from synthetic polymers [16,17]. The main advantage of applying hydrogels made from natural sources in bone engineering is that they have unique compositions that closely resemble that of the native bone extracellular matrix, which can mimic the real biological microenvironment in bone defect [18]. This reduces inflammation and immune body reaction to the implant while facilitating cell attachment, spreading and proliferation on their matrixes during the initial stage of bone healing, which induces faster bone regeneration.

Hydrogels made from natural polymeric sources have shown weak mechanical properties combined with high degradation rates, which limit their usage in the field of hard tissue engineering. Currently, inorganic materials, such as hydroxyapatite prepared in the form of particles or fibers are added to the natural polymeric structures to create composite hybrid hydrogels with improved mechanical properties, more suitable degradation rate, and closer structure to the natural bone [19–23]. It is anatomically considered a composite hybrid material consisting of a natural polymer (collagen) entangled with an inorganic component (hydroxyapatite crystals). In addition, natural polymers like alginate can support endochondral ossification but they cannot induce angiogenesis, osteogenesis and bone regeneration, as they are bio-inert and accordingly unable to integrate well with normal bone [24,25]. On the other hand, hydroxyapatite is bioactive, osteoinductive, and osteoconductive [26–28]. It has a great capacity to stimulate angiogenesis, and osteogenesis and accelerate bone formation besides mineralization. Therefore, it is expected that combining alginate with hydroxyapatite will produce suitable injectable hydrogel for hard tissue regeneration, which is characterized by optimized mechanical properties besides excellent capacity for bone regeneration and defect reconstruction. The addition of hydroxyapatite particles to injectable alginate can accelerate the in-situ gelling mechanism due to hydrogen bond formation between hydroxide groups of hydroxyapatite and carboxylic acid groups of the polymer. Moreover, alginate can be ionically cross-linked by mono, di, or multivalent ions, which can further improve its mechanical and degradation properties [5,29]. Also, ionic crosslinking can provide alginate-based hydrogels with excellent anti-bacterial properties [30]. Bio-natural injectable hydrogels are currently attracting much interest because they can adjust, correct, and adapt to irregular bone defects and mimic the composition of natural bones. To our knowledge, the previous studies of hydroxyapatite/alginate compositions are mainly based on chemical sources, while that based on hydroxyapatite/alginate composites from natural resources lack in-vivo testing [31]. Accordingly, the main goal of the current study is to fabricate injectable hydrogel pastes based on the inorganic and organic composition of natural resources enriched with valuable trace elements. Accordingly, the main objective of the study is to prepare and characterize natural injectable hydrogels using various amounts of alginate, that were obtained from brown algae and were cross-linked by calcium ions, which were combined with nano-hydroxyapatite derived from eggshells. The viscosity, setting time and mechanical properties of the prepared injectable hydrogels were studied. The simulated body fluid was used to evaluate the in-vitro, water absorption, degradation and bioactivity of the hydrogels. Moreover, the effect of the prepared sample on cell viability and attachment was evaluated. The bone healing capacity and safety evaluations of injectable hydrogels were examined via the injection of the hydrogels in the rabbit bones. Fabricating bio-natural injectable hydrogels paste based on natural resources enriched with valuable trace elements (originated from eggshells) and has both inorganic (Biogenic hydroxyapatite prepared by co-precipitation methods) and organic (Alginate: derived from brown sea algae as a polysaccharide polymer) components has a great potential to regulate, correct, and adapt to irregular bone defects besides their capacity to stimulate bone regeneration by mimicking the composition of natural bones hydroxyapatite/alginate compositions mainly based on chemical sources. However, the main hydroxyapatite/alginate compositions mainly based on chemical sources. However, the main goal of this current study is fabricated injectable hydrogels past based on natural resources enriched with valuable trace elements for both of inorganic and organic composition such as alginate (Alg) that derived from brown sea algae as a polysaccharide polymer. In addition, nano biogenic-hydroxyapatite (HA) as inorganic compound prepared from eggshells by co-precipitation methods. Currently, Bio-natural injectable hydrogels are currently attracting a lot of interest because of their capacity to regulate, correct, and adapt to irregular bone defects as well as their capacity to mimic the composition of natural bones.

2. Materials and methods

2.1. Materials

The materials used are:

Calcium chloride dihydrate $CaCl_2{\cdot}2H_2O$ (Sigma), was chosen as a source for Ca^{2+} ions (cross-linker), Molecular Weight 147.01, EC Number, MDL number, PubChem Substance ID, Sodium alginate salts, from brown algae, purchased from (Sigma-Aldrich) Germany, A1112–100 G, P code 10011146, CAS 9005-38-3, Lot # 051 M 1684 V. Reagent-grade NaCl, $NaHCO_3$, KCl, $Na_2HPO_4.2H_2O$, $MgCl_2.6H_2O$, $CaCl_2$, Na_2SO_4, Na_2HPO_4, KH_2PO_4 and HCL which were used for the preparation of biological fluids (SBF) solution utilized for evaluations the bioactivity behaviour of the developed injectable hydrogels BP-B.

2.2. Methods

2.2.1. Preparation of nano-hydroxyapatite (n-HA) from eggshell

Nano biogenic hydroxyapatite from (eggshell) with a particle size ranging between 35 and 122 nm prepared according to Naga et al. procedures [32].

2.2.2. Preparation of injectable hydrogel Alg/n-HA

A 3 % aqueous solution of Alg was prepared by dissolving 3 g Alg in 80 ml distilled H_2O + 20 ml $CaCl_2.2H_2O$ as a cross-linker. The concentration of Alg (3 %) was chosen on the bases of a previous study [26], and the viscosity at room temperature for Alg (3 %) equal 230 (Cp). Different proportions of the prepared Alg solution ranging between 1, 2 and 4 ml were used to prepare the Alg/n-HA paste' batches, Table 1. The advantage of using gelling agents (alginate salt) is to transmit viscous flow on wetting. The present study, converts the nano-hydroxyapatite powder into a uniform injectable paste, biocompatible, while it didn't affect the setting properties of the hydrogel. On the other hand, it has manifested toxicological safe [33] and its pharmacologically helpful impact on bone substitution [34].

2.2.3. In-vitro test

In order to evaluate the samples' in-vitro bioactivity, the formation of an apatite layer over the examined samples (BP-B) injectable hydrogel

Table 1
The batch composition for the Alg/n-HA injectable hydrogel.

Alg/n-HA samples code	Alginate, ml	n-HA, g	Dis. H_2O, ml
BP-A	1	5	1.5
BP-B	2	5	1
BP-C	4	5	0.5

sample surface after immersion in simulated bodily fluid (SBF) at 37 °C was examined. SBF solution having pH 7.4 was composed based on the protocol of Kokubo and Takadama [35]. After immersion of the samples in SBF solution for (1,3,7, 14, 21 and 28 days) with a solid/liquid ratio of 1.5 mg/ml at a constant medium, the concentration of the calcium and phosphorus ions was measured by inductively coupled plasma–optical emission spectrometry (ICP–OES) (5100 ICP–OES torch, Agilent, Australia). The pH values were also measured for the abovementioned immersion times. Three measurements for each time were performed, and the average value was determined. Additionally, a scanning electron microscope (SEM- Quanta FEG 250, Netherlands) with an attached energy dispersive x-ray spectroscopy (EDS) unit was used to examine the microstructure of the apatite layer formed on the sample surface.

The produced BP-B sample injectable hydrogel weight loss % in phosphate buffer saline solution (PBS) at pH = 7.4 for 1 up to 4 weeks at 37 °C, was tested to estimate its in vitro degradability. The final weight loss of the studied samples was calculated using the following formulas Motwani et al., [36]:

$$W_L = [(W_0 - W_t)/W_0] \times 100$$

where, W_0 is the initial weight of the hydrogel sample, and W_t is the dry weight at the measured studied time (t).

The weight difference between the initial sample weight before soaking in PBS solution and its weight after immersion in the PBS was used to calculate the water absorption percentage. The excess solution was removed carefully with filter paper. The water absorption % was calculated by the following equation described by Macedo et al. [37].

$$\text{Water absorption}\% = [(W_w - W_d)/W_w] \times 100$$

where, W_d: the dry weight of the hydrogel sample and W_w: the wet sample weight after soaking for various periods in PBS solution. For three samples, the degradation and water absorption tests were repeated, and the average value was taken to guarantee the accuracy of the measurements.

2.2.4. Characterizations

The chemical composition of the n-HA was investigated using X-ray fluorescence spectroscopy (XRF, PW 2404, Malvern Panalytical Ltd., UK). The apparent porosity and bulk density of the injectable hydrogel (BP -A, BP —B, and BP —C) were estimated using the Archimedes method (ASTM C-20) [38]. The phase composition of the samples was analyzed using X-ray diffraction (XRD) using monochromatic Cu-Ka radiation (XRD, X'Pert-PANalytical, UK). The best injectable hydrogel BP-B sample was investigated with a transmission electron microscope (TEM) JEOL, JEM-2100-HR, Japan to determine the grain particle size. FTIR analysis of Alg/n-HA hydrogel (BP —B sample) was carried out using an FT/IR- 6100 Fourier transform Infrared Spectrometer from JASCO, at a range of 400–4000 cm^{-1}. The crushing strength of the Alg/n-HA injectable hydrogel was measured using a universal testing machine (Tinius Olsen 25 ST, United Kingdom, Twin column Load cell 25 KN, serial no. ST-AF-02026 GB, Honey Crock Lane, Salford, surrey RH1 DZ) with a crosshead speed of 0.5 mm/min, as stated by DIN EN 6872 [39]. Then-HA powders were sterilized under ultraviolet (UV) light 2028 ABOUOKEILET AL for 30 min in a laminar flow before usage. Viscosity measurements were studied at different temperatures of 25, 37, 50, and 60 ^{o} C for the polymeric (Alg). The Viscosity of the polymeric (Alg) solutions was measured using a Brookfield Viscometer (Model DV-III Ultra, UK). To examine the effect of adding polymeric (Alg) solutions to the nano-hydroxyapatite powder, their mixtures were placed in the built-in stainless-steel container attached to a temperature controller. Then, measurements were done using the S23 spindle at 30 RPM under uniform temperature. While the setting times test was done according to International Standards ISO 9917-1 (2003 E) [40].

2.2.5. MTT (cytotoxicity) assay test

All cytotoxicity studies were performed on bone osteosarcoma cell line (HOS), which were cultured in a complete growth Dulbecco's modified Eagle's medium (DMEM) supplemented with 10 % FBS, L-glutamine (2 mM), streptomycin (100 μg/ml), and penicillin (100 IU/ml) in the CO_2 incubator at 37 °C, 5 % CO_2, and saturating humidity. For evaluation of Alg/n-HA (BP —B sample) injectable hydrogel cytotoxicity, cells were seeded at a concentration of 5000 cells per well into a 96-well tissue culture plate and incubated overnight under the conditions described above. The cells were treated with samples at concentrations (200, 100, 50,25 μg/ml) for 48 h. After the incubation, 40 μL from MTT was added to each well and incubated for 4 h. Afterwards, 100 μL of DMSO was added to extract formazan produced by living cells. The absorbance of DMSO has measured at the wavelength 595 nm by a plate reader (Lab systems Multi-scan MS). The percentage of cytotoxicity [41] was calculated using the following equation:

$$\%\text{Cytotoxicity} = [1 - (\text{AVx}/\text{AVNC})] \times 100$$

2.2.6. Cell attachment

To explore the cell adhesion on the surfaces of Alg/n-HA injectable hydrogel, the injectable hydrogel samples were placed and fixed in the bottom of each well of a 24-well plate and then sterilized with UV light in laminar flow for 25 min. Posteriorly, bone osteosarcoma cell line (HOS) from American Type Culture Collection (ATCC) were then seeded onto the surfaces of the samples at a density of 20×10^3 (200 μl of cell suspension) and cultured with Dulbecco's Modified Eagle's Medium (DMEM; Invitrogen, Carlsbad, CA, USA) supplemented with 10 % fetal bovine serum (FBS; Hyclone, Logan, UT, USA) and 1 % penicillin/streptomycin (P/S; Gibco, Grand Island, NY, USA) in a humidified incubator at 37 °C and 5 % CO_2. Before cell culture on the material surface, at 70 % assemblage, the cells were harvested by trypsinization and used for experiments. Samples containing cells were taken out after incubating the plates for 48 h, rinsed twice with phosphate-buffered solution (PBS) to remove the non-attached cells, and subsequently fixed with 2.5 % glutaraldehyde overnight for 2 h. at 4 °C. Then, the samples were rinsed in 0.1 M PBS, transferred to the critical-point dryer, and dried with CO_2. The dried samples were sputtered with a thin layer of gold for monitoring of cell morphology using an electronic microscope (QUANTA FEG250) at an acceleration voltage of 20.00 kV.

2.2.7. Animal model design

Twenty-one healthy adult male white rabbits with an average weight ranging between 1.9 and 2.5 kg were appointed for the experiments. The rabbits were treated according to the ethical guidelines of the International Animal Care and Use Committee (IACUC), National Research Centre of Egypt with approval number (15/039). For the in vivo study, a 5 mm cavity was created in the midst of each rabbit's femur as in Fig. 1. The rabbits were assorted randomly into 2 categories.

Category 1 (Control): Consisted of 7 non-implant rabbits, living in the same conditions as the implanted rabbits.

Category 2: Consisted of 14 rabbits having femur holes implanted with sanitized injectable hydrogel Alg/n-HA (BP-B). This category is split into two subgroups:

- Ten weeks post-surgery subgroup: containing 7 rabbits that were sacrificed after 10 weeks post-operation.
- Twenty weeks post-surgery subgroup: containing 7 rabbits that were sacrificed after 20 weeks post-operation.

2.2.7.1. Follow up postoperative. Following up the postoperative consists of two main aspects; 1) femur bone analyses and 2) blood biochemistry examinations.

2.2.7.1.1. Femur bone analysis:. a) Clinical evaluation

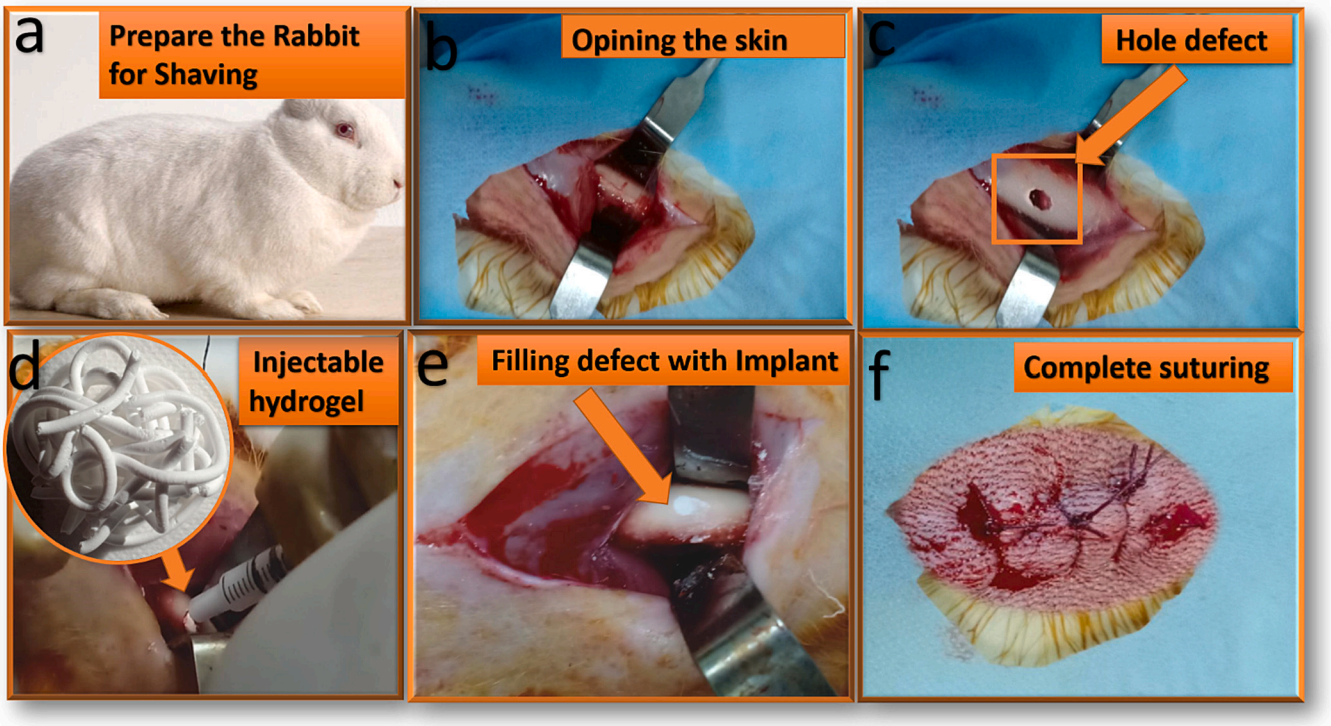

Fig. 1. Represents the surgical procedures.

Attention was paid to the rabbits to be sure that they haven't any general or topical inflammation or complexities after surgery and throughout the study interval.

b) Radiology test

The implanted sites were imaged by X-ray along the sidelong and anteroposterior (AP) sites to define the variations that took place in the bones during the study. Mobile X-ray Apparatus was utilized for the study.

c) Bone mineral density test (BMD)

Bone density measurement is used to personate and monitor the curing of skeletal diseases like osteoporosis and so on. A dual x-ray absorptiometry (DEXA) machine (Norland Medical Systems Inc., XR-46, Fort Atkinson, Wisconsin, Model 434 A063, USA) was employed for BMD analysis. Three bone samples are examined simultaneously and in the same scan.

d) Scanning electron microscope and energy-dispersive X-ray analysis (SEM and EDS)

The recently-formative bones were examined by SEM (JEOL JSM-T20) coupled with EDS Unit to assess the bone's calcium/phosphorus ratio.

e) Histologic estimation for bone renovation

For the histology estimation, samples were outfitted according to the method explained by Banchroft et al.; 1996 [42]. The samples were examined by the naked eye, then by using a light microscope (Olympus BX61, Hamburg, Germany) connected to a high-resolution digital camera (Olympus, E330, Imaging Corp).

f) Blood biochemistry tests

The implanted rabbit's pathological attitudes were tracked by biochemical tests, which embraced kidney and liver tasks, antioxidant estimation, free radical biomarker, tumor markers, erythrocyte (RBC), hemoglobin level (Hb), platelets count (PLT), and leucocyte count (WBCs).

g) Statistical analysis

The results of the implanted rabbits' group and the control rabbits' group were compared using the Program IBM SPSS statistical package Version 21.0 US. The results data were presented as mean values ± standard deviation (SD). Comparison between the two groups was performed using an independent *t*-test and the *p*-value is considered statistically considerable if ≤ 0.05.

3. Results and discussion

3.1. The chemical composition of the nano-hydroxyapatite powder from eggshell

The chemical composition of the n-HA produced from eggshells, as revealed from XRF analysis, includes CaO and P_2O_5 as main oxides. In addition, essential trace elements such as Sr, Zn, Cu and Ce in addition to the main components; calcium and phosphorus oxides (Table 2). Since natural HA contains trace elements similar to the elemental composition of human bone, accordingly it is a non-stoichiometric composition compared to synthetic HA [43]. It is well known that the presence of vital trace elements in the HA can accelerate and improve bone growth. For example, in vitro studies have demonstrated that biomaterials enhanced with Sr improved both the bioactivity and osteoblast adhesion, as well as the proliferation, and differentiation more than materials lacking Sr [44,45]. Moreover, in vivo studies indicated better new bone formation at the bone-implant interface surface, together with accelerated healing, and osseointegration compared to Sr-free materials [46,47]. Also, a lot of studies have indicated the advantages of the presence of Zn on bone remodelling, bone matrix synthesis, and

Table 2
Chemical composition of hydroxyapatite powder prepared from eggshell.

Chemical composition												
Oxide (wt%)	**CaO**	**P_2O_5**	**SiO_2**	**MgO**	**SiO_3**	**Al_2O_3**	**K_2O**	**Fe_2O_3**	**Cl**	**LOI**		
	70.85	27.18	0.26	0.23	0.11	0.08	0.03	0.02	0.02	1.22		
Trace elements (ppm)	**Sr**	**Zn**	**Cu**	**Ce**	**Zr**	**Ni**	**Co**	**La**	**Ga**	**Te**	**Ba**	**Cr**
	156.6	14.2	5.9	23.2	1.8	0.5	3.0	19.5	0.2	10.7	8.4	1.4

mineralization in growing rats' bones [48]. It also found that the regulation of bone formation and skeleton development is greatly influenced by copper [49]. While the presence of Ce improved the angiogenic and osteogenic characteristics and has antibacterial, anti-inflammatory and antioxidant effects [50].

3.2. Characterization of alginate/n-hydroxyapatite hydrogel

3.2.1. Microstructure of prepared injectable hydrogel

To select the optimum conditions for the control of and regulate the initial plasticity and injectability and maintain the shape stability of the injectable hydrogel and help in handling the injectable hydrogel; the hydroxyapatite powder was converted to an injectable form by adding different amounts of the alginate as illustrated in Table 1. The SEM as in Fig. 2 of the fabricated pastes showed that with increasing alginate content, the injectable hydrogel (BP-A) sample was mostly composed of hydroxyapatite and contained comparatively small amounts of alginates when compared to injectable hydrogel (BP-C) samples.

On the other hand, the apparent porosity the compressive strength and setting time measurements, Table 3, illustrated that BP-C had a faster setting time (9 mins) and a higher compressive strength (7.9 MPa) than BP-A, which had a slower setting time (20 mins) and a lower compressive strength of (5.9 MPa). Otherwise, the paste (BP-B) sample had an appropriate setting time for injecting (13 mins), and compressive strength reached 6.3 MPa.

Additionally, visual observation as in Fig. 2 during the rheological test showed that the BP-A sample possessed high fluidity, fragility and brittle appearance and is difficult to handle. While the injectable hydrogel BP-C sample failed to apply due to low plasticity and its phase separation. Accordingly, the injectable hydrogel (BP-B) was the most suitable paste to be used in an injectable form, as it has an appropriate setting time and compressive strength, and it does not suffer from non-phase separating during injection from the syringe. In addition, it keeps the stability of the injectable shape after injections from the syringe as in Fig. 2.

3.2.2. Rheological and mechanical measurement

The results showed that the addition of polymeric gelling agents (Alg) increased the net viscosity at the same temperature for all the injectable hydrogel BP-A and BP-B, and BP-C. It also noticed that the increase in the temperature up to 50 °C decreased the viscosity. At 60 °C all the pastes' viscosity was decreased, which may be due to the solidification of the pastes. The final results confirmed that the viscosity of the injectable hydrogel (BP-B) is the suitable and easier one to handle where normal suitable values of viscosity in the range of 100–2000 (Pa·s) is generally acceptable [51,52]. As BP-B injectable hydrogel possessed a suitable setting time; adequate slow for the surgeon to complete the implantation, yet adequate speedy for the completion of the surgery in time without both shrinkage and cracking the paste; we chose it as the best composition for carrying up the remaining tests of our study. The results agree with the results of Bendtsena, et al., 2017 [53].

The apparent porosity and the bulk density of different injectable hydrogel were determined as clarified in Table 3. The specimens with the lowest content of cross-linked alginate (BP-A) and highest water content showed the highest Apparent porosity (54.50 ± 4.13 %) and the lowest bulk density (1.01 ± 0.11). While the specimens with the highest content of cross-linked alginate (BP-C) and lowest water content showed the lowest Apparent porosity (19.03 ± 1.97 %) and the highest bulk density (2.03 ± 0.04). According to the abovementioned results, the injectable hydrogel (BP —B) was the most suitable paste to be used in an injectable form.

3.3. Characterization of alginate/n-hydroxyapatite (BP-B) injectable hydrogel

3.3.1. XRD analysis

The produced alginate/n-hydroxyapatite injectable hydrogel was subjected to an X-ray diffraction (XRD) examination, which revealed that the HA had the standard diffraction pattern of a well-crystalline HA phase. The HA-produced X-ray diffraction values can be compared to those in the JCPDS (005–0586) standard data, Fig. 3 (a). Otherwise, due to the amorphous nature of the alginate, its XRD patterns could not be identified.

3.3.2. IR analysis and TEM

Fig. 3 (b) illustrates the FT-IR spectra of the nano biogenic HA powder calcined at 900 °C for 2 h (black spectrum). It is easy to distinguish the characteristic bands of the phosphates group $(PO_4)^{3-}$ at (1025, 600 and 565 $cm^{-1}(\upsilon_4)$, 469.7 $cm^{-1}(\upsilon_2)$, 964 cm^{-1} symmetrical stretching mode (υ_1), and1090 cm^{-1}asymmetric stretch mode (υ_3)

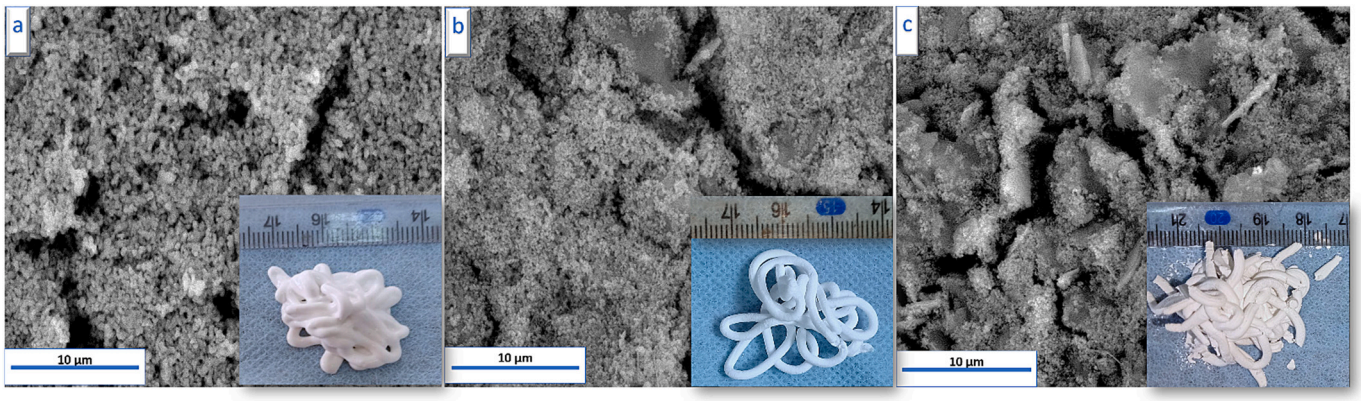

Fig. 2. SEM micrographs for the prepared injectable hydrogel a) BP -A, b) BP -B, and c) BP -C.

Table 3
Effect of increasing of alginate polymer addition on the apparent porosity, bulk density, setting time, compressive strength and viscosity on the produced injectable Alg/n-HA hydrogel.

Samples	Apparent porosity, %	Bulk density, g/cm^3	Setting time, min.	Compressive strength, MPa	Viscosity (Pa—S) at different Temperature			
					25 °C	37 °C	50 °C	60 °C
BP- A	54.50 ± 4.13	1.01 ± 0.11	9	7.9 ± 2.4	865	815	799	755
BP-B	29.93 ± 0.89	1.97 ± 0.02	13	6.3 ± 1.8	1960	1392	1370	1350
BP-C	19.03 ± 1.97	2.03 ± 0.04	20	5.9 ± 1.29	3800	2890	2046	1788

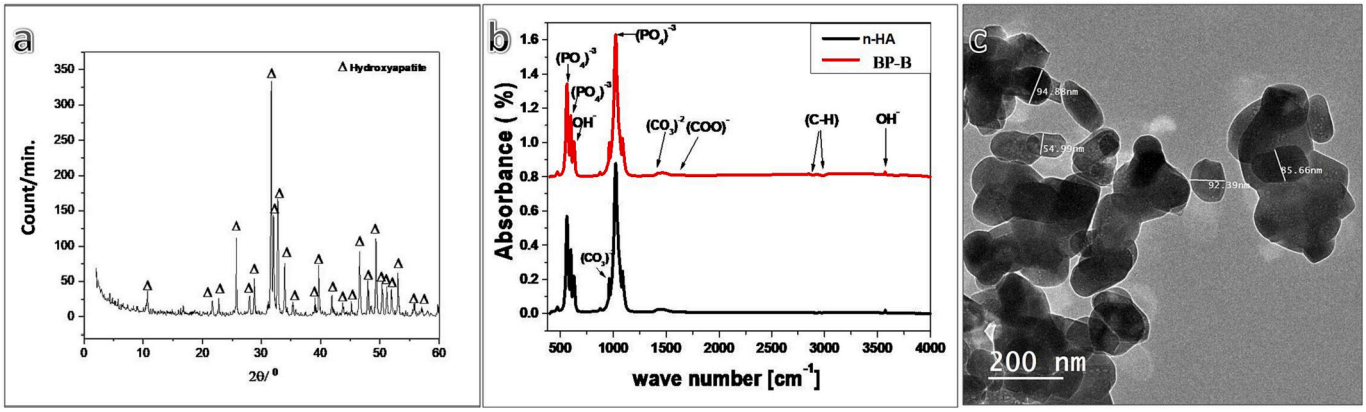

Fig. 3. X-ray diffraction patterns (a); FTIR (b); TEM image for the injectable hydrogel BP -B hydrogel (c).

[54,55]. The hydroxyl group $(OH)^-$ band is found as a stretching mode band at 3572.23 cm^{-1} and 630 cm^{-1}) [56]. While, small bands appeared at 1467.86, and 876.25 cm^{-1} corresponding to vibration mode (υ_3), (υ_2) of carbonate group $(CO_3)^{2-}$. The carbonate group appeared because of the calcination process of the nano HA produced from eggshells.

Fig. 3 (b) indicates the FT-IR of the sample BP-B injectable hydrogel (red spectrum). It is easy to recognize the peculiar bands of alginate salt (Alg) at 1628 cm^{-1} for the asymmetric carboxyl $(COO)^-$ and 1467.06 cm^{-1} for symmetric carboxyl $(COO)^-$ bands. Also appeared an interaction between the Ca^{2+} in the cross-linked calcium chloride ($CaCl_2$) and the carboxyl groups $(COO)^-$in the alginate (Alg) structure called "egg box" [–COO^-]–Ca^{2+}–[–COO^-] [chelating structure, which could be used as useful bands to follow up the changes in the structure of poly alginate]. These linkage sites work as nucleation sites for attaching nano-hydroxyapatite during the mixing of the injectable hydrogel BP-B [57]. While, the stretching vibration for $(C—H)_2$ bands appeared at 2851.02, 2924, and 1628 cm^{-1}.

Based on the TEM analysis of the Alginate/n-hydroxyapatite injectable hydrogel, indicated that the particle size was in the nano-size and it ranged from 54.99 to 94.88 nm Fig. 3 (c).

3.4. *In-vitro study*

The incubation of the injectable hydrogel (BP-B) in phosphate buffer saline solution (PBS) at pH = 7.4 for 1 up to 4 weeks, indicated that the weight loss increased gradually from the first week of the incubation period to the third week to reach 13.08 % of its initial weight, and then slightly decreased at the fourth week to 12.47 %, Fig. 4 (a). It has been shown that the tendency of the biomaterials to degrade has an important effect on the development of implantation sites on the biomaterial framework, which stimulate the growth of new bone and promote bone substitution and regeneration [26,36].

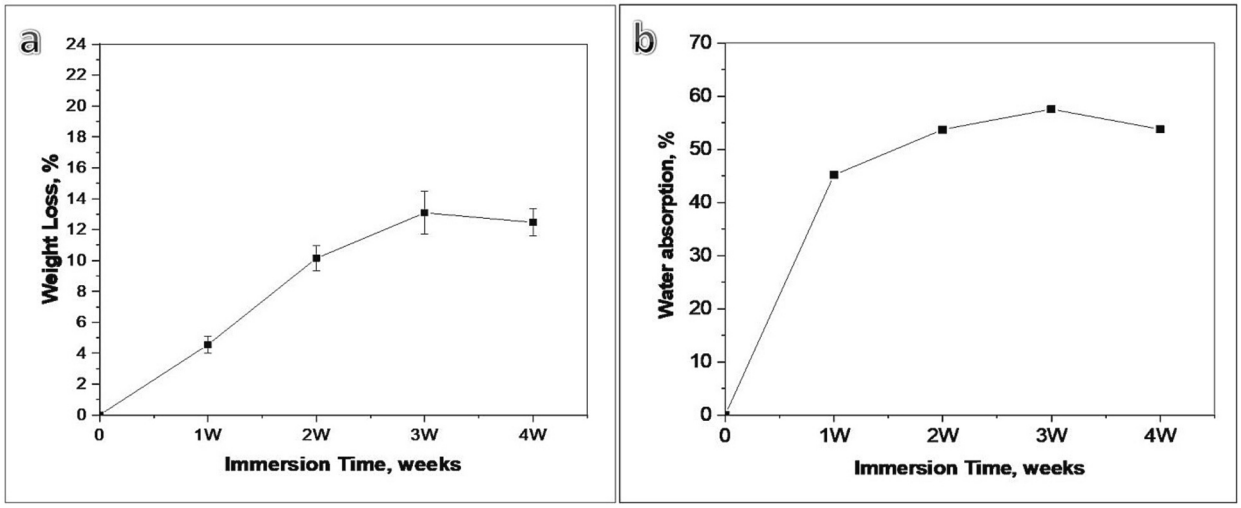

Fig. 4. Showed (a) weight loss % and (b) water up take % versus different immersion times (weeks) in PBS for injectable hydrogel BP-B.

Water absorption is one of the most significant features of hydrogel polymers utilized in tissue engineering applications. It offers the aqueous environment required for biomaterials to encourage cell adhesion, growth, and differentiation [58]. Fig. 4 (b) showed the water absorption of the developed injectable hydrogel BP-B increased gradually from the 1st week of immersion time to the 3rd week to reach 57.58 % of its initial weight, followed by a small decrease in the fourth week to reach 53.78 %. The water absorption of injectable hydrogel BP-B increased gradually and then nearly fixed at a long immersion period due to many reasons; 1) the presence of Alginates which are characterized by hydrophilic properties, including two main functions groups; (COOH) that interact directly with water (HOH), and (COO^-) function group that cross-linked with Ca^{2+} ions [knowing as an egg-box structure] with increase the time of immersion Ca^{2+} ions release and replaced by a hydrogen bond (H^+) from water solution [26,59]. 2) OH^- function group in hydroxyapatite (HA) also played a part in water absorption.

Fig. 5 displays the change in SBF composition and its corresponding pH variation after the immersion of injectable hydrogel BP-B paste for 28 days. As illustrated, from the initial day to the 3rd immersion day, Ca^{2+} and PO_4^{3-} concentrations in SBF highly decreased from 146 mg/l, and 60 mg/l to 86 mg/l and 42 mg/l, respectively, followed by an increase on the 7th immersion days. Then a gradual decrease on the 14th day was noticed. While, on the 21st immersion day, another increase was observed. At the end of the immersion period, a decrease in Ca^{2+} and PO_4^{3-} concentrations were detected reaching 97 mg/l and 48 mg/l, respectively. The changes in the Ca^{2+} and PO_4^{3-} ions concentration in the SBF solution could be attributed to the occurrence of two processes. The first is the degradation process, which took place at the initial period of immersion and resulted in an increase in the ions concentration. And the second is the development of the hydroxyapatite particles on the sample surfaces, which caused the Ca^{2+} and PO_4^{3-} ions concentration to decrease. It was noticed that the measured pH values for the studied injectable hydrogel at all immersion times are quite near to the levels advised for biomedical applications.

The bioactivity of the studied injectable hydrogel BP-B was evaluated by SEM examination. The SEM image reveals that before immersion in SBF solution; the material had no crystalline HA formation on its surface Fig. 6 (a). After 28 days of immersion in SBF, the surface of the injectable hydrogel was completely covered with well-crystalline apatite particles on its surface, Fig. 6 (b). Moreover, the surface of the fabricated injectable hydrogel BP-B was subjected to an EDS examination before and after immersion in SBF solution. The results revealed that the existing Ca and P elements after immersion in SBF had a molar ratio of ($Ca/P = 1.65$) which is near to the hydroxyapatite ratio ($Ca/P = 1.67$), and higher than that obtained for the Ca/P before immersion in SBF solution ($Ca/P = 1.54$).

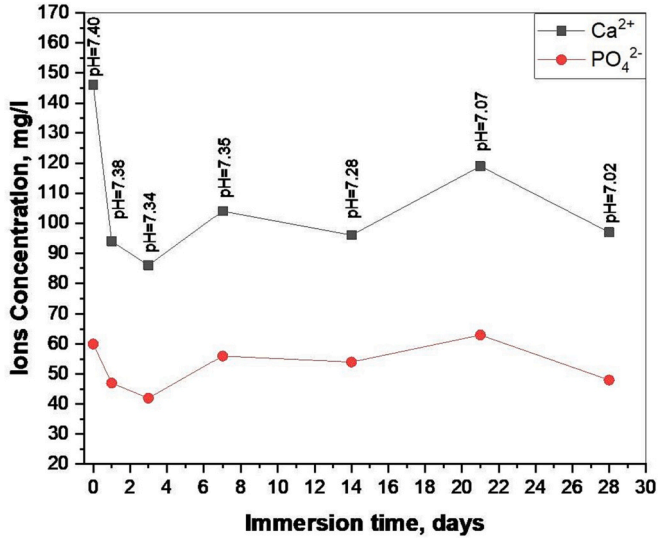

Fig. 5. The mean values for Ca^{2+} and PO_4^{3-}ion' concentrations (mg/l) for the injectable hydrogel BP-B immersed in SBF, versus different immersion times.

3.4.1. *In vitro cells based assays*

In vitro cell-based assays are considered valuable techniques that can provide more information about the ability of cells to interact with material surfaces through attachment, spreading, reproducing, and differentiation. This can help determine the materials' overall biological behaviour and predict their capacity for bone regeneration in animals. In vitro, cell-based assays resemble and mimic the in vivo environment to a greater extent. Hence, they are used to assess cell viability, attachment, collagen production, and mineral deposition in the bone matrix, thus, providing evidence of in vitro bone-like tissue formation.

The cytotoxic effect of the Alg/n-HA injectable paste on bone osteosarcoma cell line (HOS), was evaluated by subjecting the cells to different concentrations (200, 100, 50,25 μg/ml) of Alg/n-HA injectable hydrogel (BP —B sample) for 48 h. The percentages of cell viability at these concentrations were provided in Fig. 7 (a). It is seen that cell viability is high at all concentrations. The measured percentage of cells viability at 200, 100, 50 and 25 μg/ml is 89.5 ± 3, 96.5 ± 4, 100.5 ± 5 and 104.3 ± 6, respectively. Results indicated that the sample is biocompatible and has no toxic effect on cells. Fig. 7 (b) shows the morphology of treated cells with different sample concentrations (100 and 200 μg/ml) compared to untreated cells. Both treated cells and normal untreated cells had similar morphology.

Cell attachment and spreading on the sample surface are provided in Fig. 8 (a-d). It is seen that cells were able to adhere, attach and spread on the surface (indicated by black arrows) forming a sheet or a layer that almost covered the sample, some small grooves were also noted, which were filled with cells (indicated by red arrows). Moreover, as indicated by EDX analysis (data not shown), spherical carbonated apatite particles were also formed on the surface of the sample. These apatite particles originated due to cell-induced minerals deposition forming apatite nodules [60]. That apatite particles are also driven by back-precipitation of Ca^{2+} and PO_4^{3-} from surrounding tissue culture media. These (Ca^{2+} and PO_4^{3-}) ions were formerly released from the dissolution of biogenic hydroxyapatite inside the sample.

3.5. *In-vivo evaluations*

3.5.1. *SEM/EDX*

3.5.1.1. Ten weeks post-surgery for injectable hydrogel BP-B and control group. SEM images taken at different magnifications for defect areas grafted with injectable hydrogel BP-B are shown in Fig. 9 (a-f). A large part of the defect area was closed and various types of newly formed bone can be detected growing at the edges of the bone defect as seen in Fig. 9 (a) and (b). They included; 1) mature bone showing well-developed Haversian systems as noticed through an area marked by a red star indicating that active remodelling is being carried out at this early stage of bone healing, 2) bone tissue proceeding through the progress of maturation, as evident by the formation of primary osteon structures as seen in the area identified by a yellow star, 3) immature bone known as osteoid tissue containing few osteocytes in lacunae spreading within the area indicated by a white star. This osteoid area was further magnified in Fig. 9 (c) and (d). In addition, a massive organic matrix (dark grey area donated by a black star) consisting of extensive arrays of organized collagen fibers with several hydroxyapatites (HA) crystals deposited on its surface is observed near the edge of the defect, which is fully spread and intensely propagated inside the defect. This organic collagenous matrix is magnified in Fig. 9 (e), where several hydroxyapatite crystals are seen deposited as indicated by red arrows. Moreover, the area within a red square in Fig. 9 (a) was

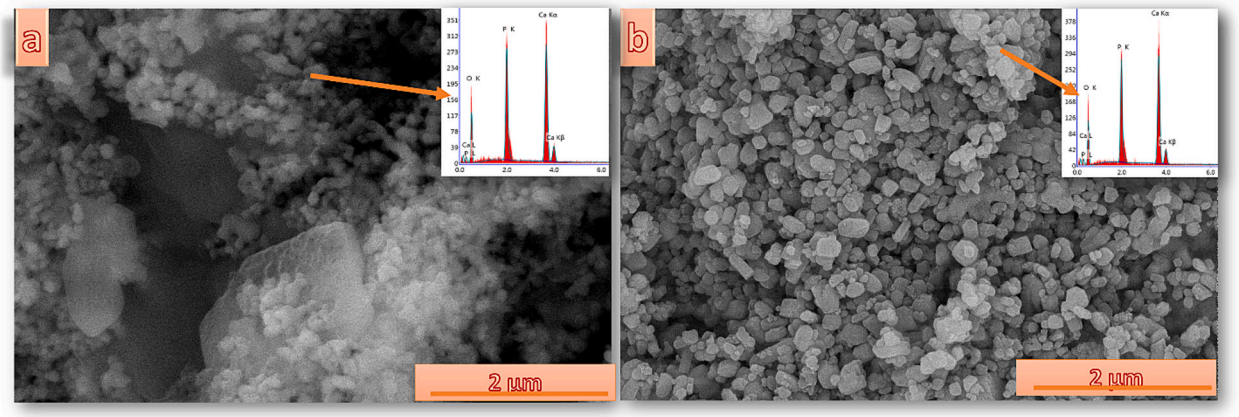

Fig. 6. SEM micrograph of injectable hydrogel (BP-B) before (a) and after (b) immersion in SBF solution for four weeks with their respective energy-dispersive X-ray analysis (EDS).

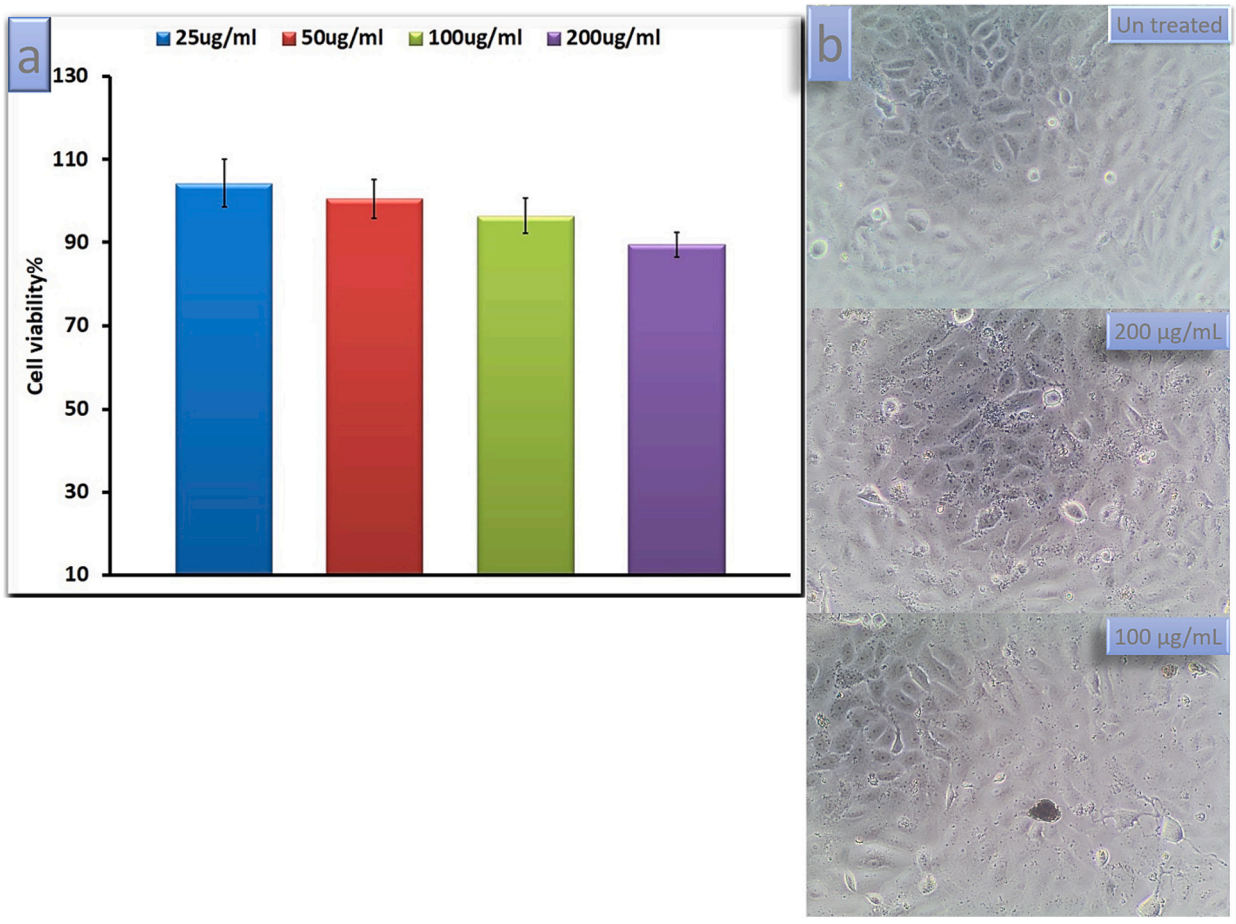

Fig. 7. Shows (a) the percentage of cells viability using different concentrations of injectable hydrogel (BP -B sample), and (b) the morphology of treated cells compared to untreated ones

magnified in Fig. 9 (f), where several osteoblasts and osteoclasts are seen sited at the edge of the healing defect indicating active bone formation and remodelling Fig. 9.

Fig. 10 shows an overview of the entrance of bone defect (a). Mineralized collagen fibers are seen attempting to bridge the remaining gap between defect edges (pointed out by the red arrow). In addition, a primary osteon structure (enclosed within a black circle) is seen to develop near the entrance. The figure also shows the inner part of defect (b), where a sheet composed of numerous gatherings of osteoblasts (surrounded by a blue square) is seen spreading on the sample as well. This indicated that the sample is considered safe and compatible with cells. Moreover, small pieces of bone fragments (indicated by blue arrows) are seen growing on the implanted sample. Taking a closer look at the innermost part of the defect area, a bone-forming cell (enclosed in a red circle) is seen anchoring its filopodia on the surface of the material (a) which indicates active engagement with injectable material. Finally, intensive mineralized collagen fibers are seen scattered deeply through the defect and on the surface of the implanted sample. They have several

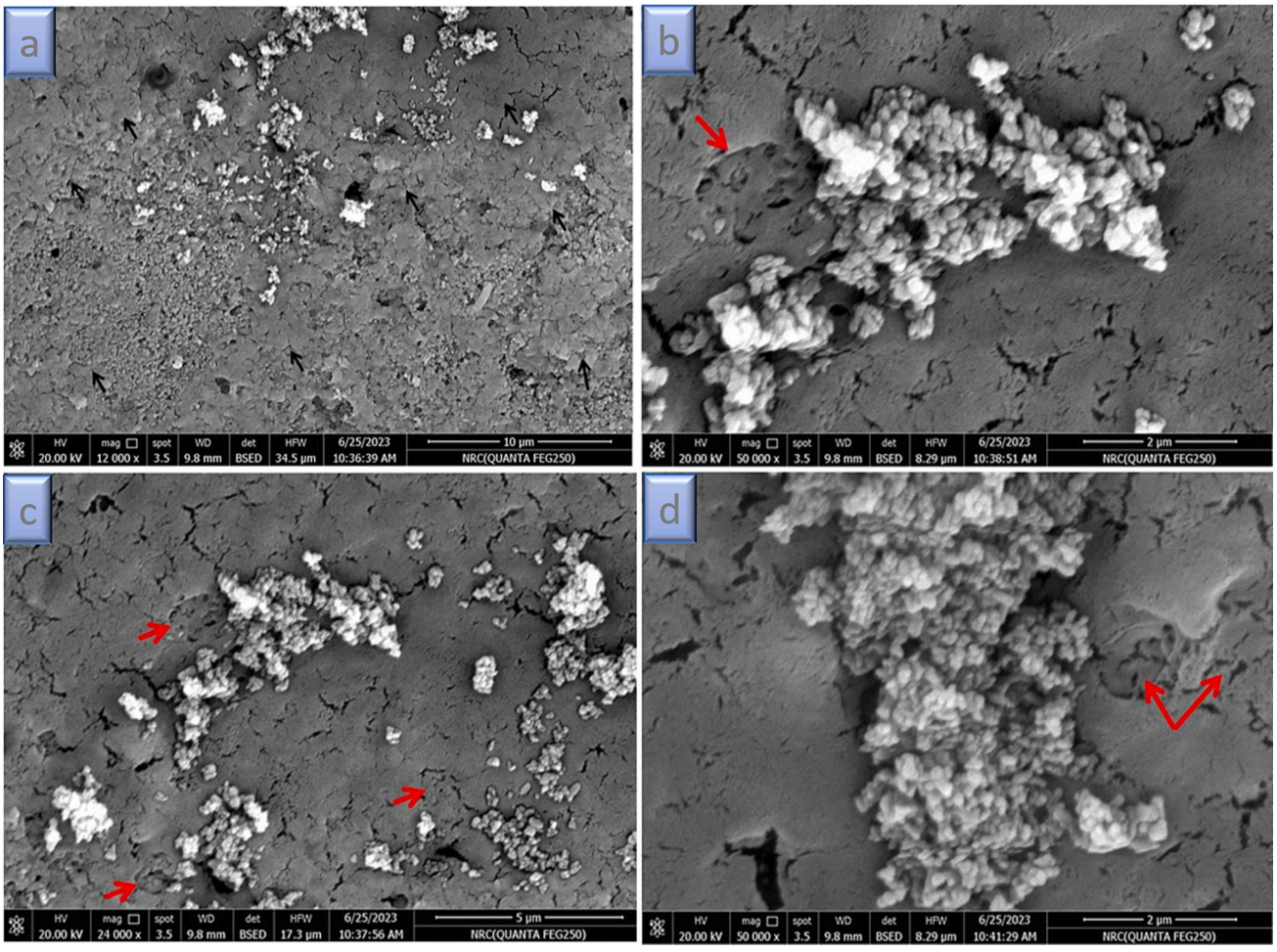

Fig. 8. Shows the interaction and attachment of cells to injectable hydrogel (BP -B) sample.

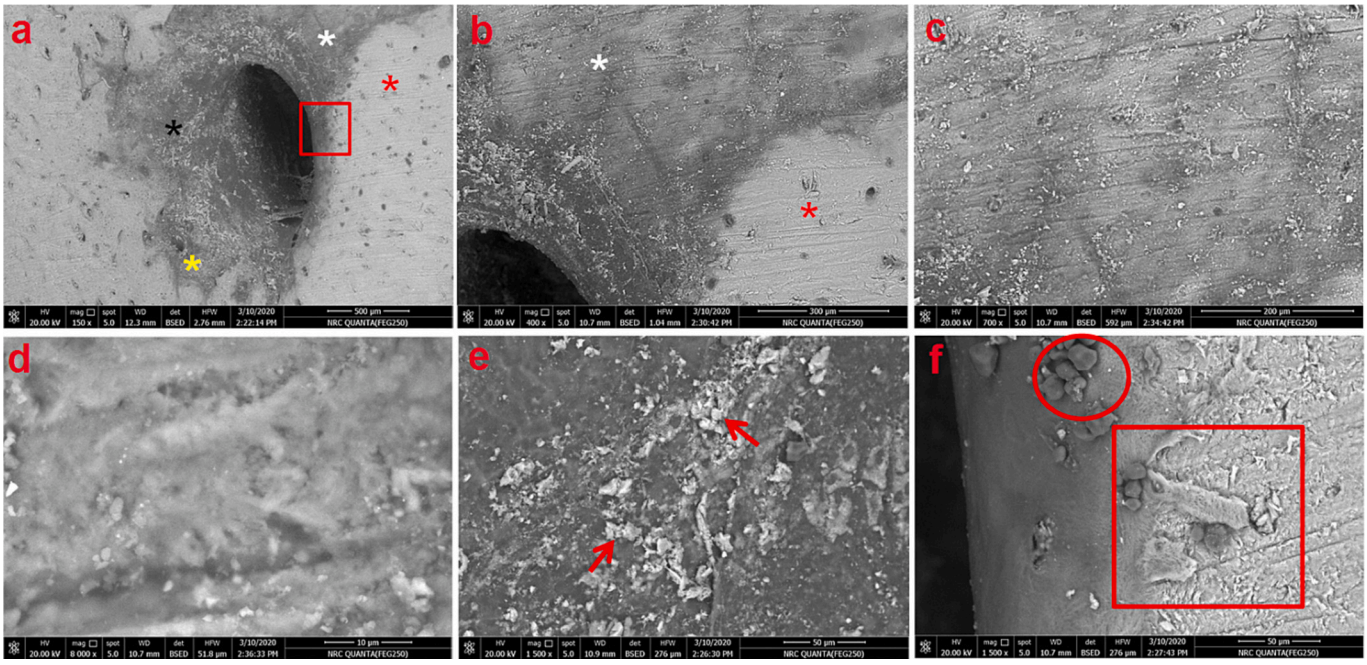

Fig. 9. SEM images taken for defect area ten weeks post-surgery at different magnification, which was filled with injectable hydrogel BP-B.

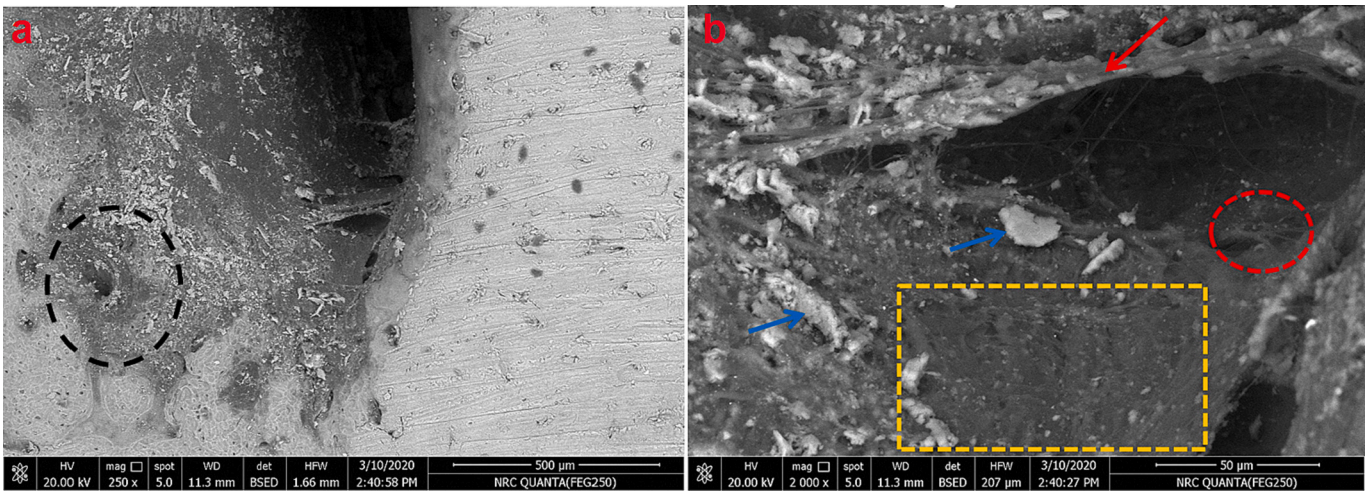

Fig. 10. Shows a magnified over view of the entrance of defect (a) and the inner deep-seated part of the defect (b).

hydroxyapatite crystals attached to their backbone. The deposited crystals originated from diffused calcium and phosphorous ion from hydroxyapatite within the injectable hydrogel Alg/n-HA sample due to its degradation and as a result of osteoclasts activity as well, which creates a surrounding environment heavily concentrated with these ions. This will lead to back-precipitation of ions and initiate the growth of hydroxyapatite crystals on collagen fibers and material surfaces as well. Moreover, collagen fibers and alginate components of the implanted composite sample have numerous carboxylate groups spreading over their backbone. These groups carry negative charges which will facilitate calcium ion's attraction from the surrounding environment and attachment to collagen and alginate backbones, which can accelerate the induction process of HA crystals as calcium ions can work as seeds for crystals growth.

EDX analysis of mature bone tissue (a), osteoid tissue (b), and organic matrix enriched with HA crystals (c) are presented in Fig. 11 (a-c). The analysis was conducted to evaluate the progress of bone mineralization of the newly developed tissue and document the improvement of bone maturation. EDX analysis has shown that calcium and phosphorous contents increased in the following order; mature bone> osteoid tissue> organic matrix. Calcium atomic % of mature bone, osteoid tissue and the organic matrix is 12.15, 8.78 and 1.69 %, respectively, whereas, phosphorous atomic % is 7.33, 5.06, and 1.08 %, respectively. At the same time, carbon atomic % for organic matrix recorded the highest value among mature bone or osteoid tissue indicating that it's richer with organic materials and not completely covered with hydroxyapatite crystals relative to mature or osteoid tissue. In addition, the calculated Ca/P atomic ratio of mature bone, osteoid tissue and organic matrix from EDX analysis is 1.66, 1.74, and 1.57, respectively. These values are very close to that of hydroxyapatite of normal bone.

SEM images taken at different magnifications for defect areas of the control group are seen in Fig. 12 (a-e). A large central portion of the defect area was not closed, the newly formed bone was seen lying down around the hole, and it started growing from the edges of the defect moving towards its central part. This newly induced bone was not entirely connected and entangled with normal old bone as the defect border was clearly distinguished from old bone by a very slight outline space. However, a small portion of the developed new bone was able to link and joined the old normal bone (area surrounded by the blue rectangle). Moreover, a few Haversian systems (pointed by yellow arrow) are noticed scattered through new bone indicating that some remodelling was taking place. In addition, a large section of defect margin was filled with organic matrix and/or occupied with parallel collagen fibers as indicated by areas enclosed within the red and yellow dotted rectangle). These areas are further magnified in Fig. 12 (b and c, respectively). Taking a closer look inside the central part of the defect area shows a fibrous connective matrix (indicated by green arrows)

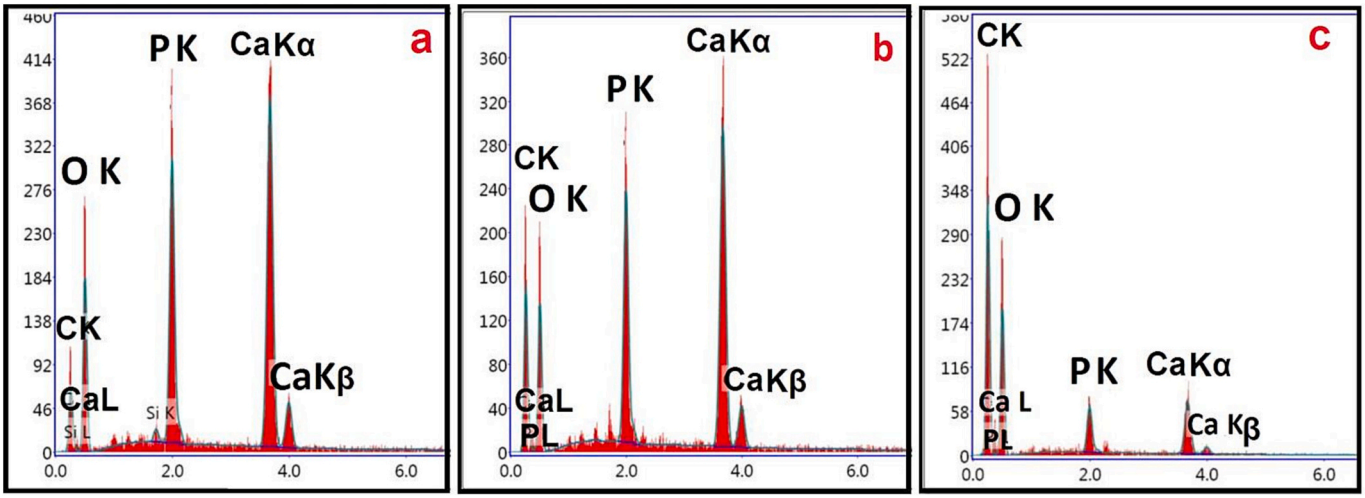

Fig. 11. Shows EDX analysis of mature bone tissue (a), osteoid tissue (b), and organic matrix enrich with HA crystals (c).

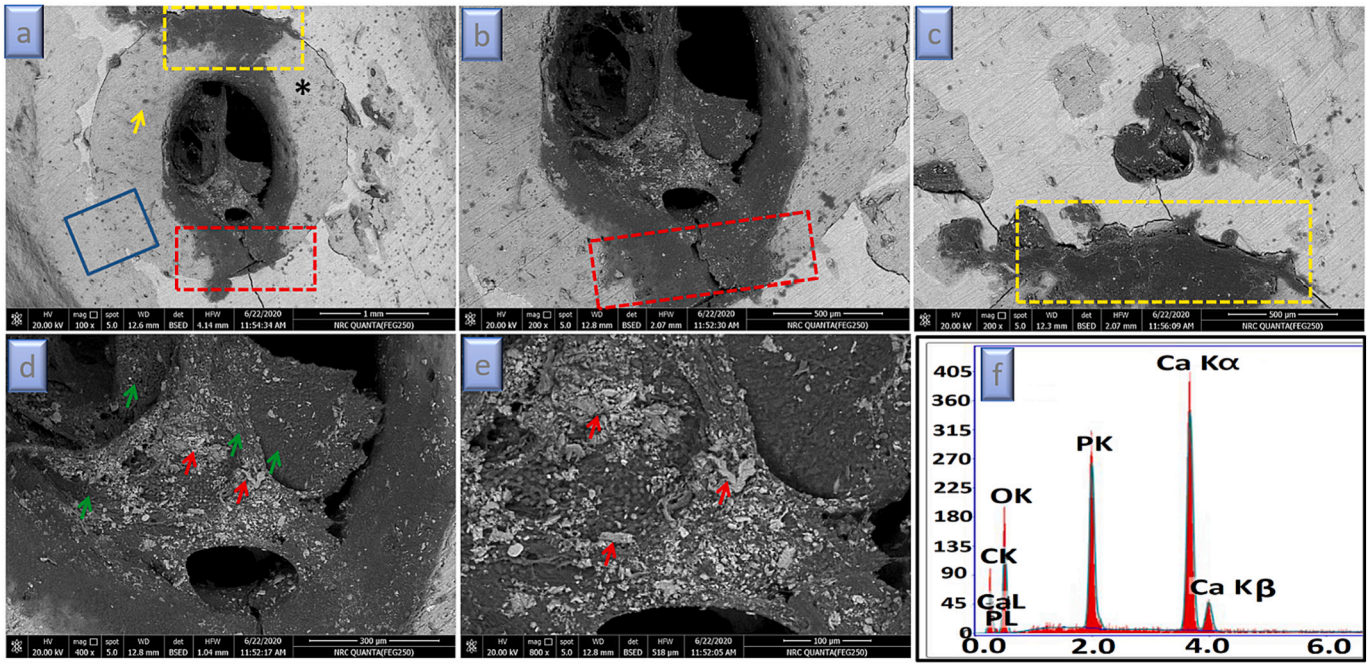

Fig. 12. (a-e) SEM images taken at different magnifications for defect areas of the control group for 10 weeks post-surgery.

filling the central hole, where a few precipitations of hydroxyapatite crystals (pointed out by red arrows) are seen on its surface. EDX analysis was carried out for newly developed bone (area marked by a black star) and is provided in Fig. 12 (f). EDX analysis has shown that Ca/P atomic ratio of newly formed bone is 1.8, which is slightly higher than that of normal bone. This higher ratio is attributed to that the newly formed bone is still not completely remodeled, as this process is responsible for trimming excess bone and creating channels for blood vessels passage to deliver food and oxygen to cells. In addition, it might be due to that the newly formed bone is not well mineralized (having reduced phosphorous content) or carbonate groups are substituting some of the phosphate groups of hydroxyapatite crystals in bone tissue.

3.5.1.2. Twenty weeks post-surgery for injectable hydrogel BP-B and control group. SEM images for the grafted defect areas with injectable hydrogel BP-B showed that it is nearly closed, only a small space is still not completely bridged as seen in Figs. 13 (a) and (b). A small piece of bone (pointed by a red arrow) is seen formed at the edge of the defect trying to connect between its borders. In addition, the newly grown bone at the defect surface is mostly converted into a well-mature and mineralized bone (areas donated by a black star) as several well-developed Haversian systems are seen scattered through bone tissue as indicated by white arrows in Fig. 13 (b). Still, very few parts of generated mineralized bone are going through maturation having limited osteon structures (area donated by a white star). At this advanced stage

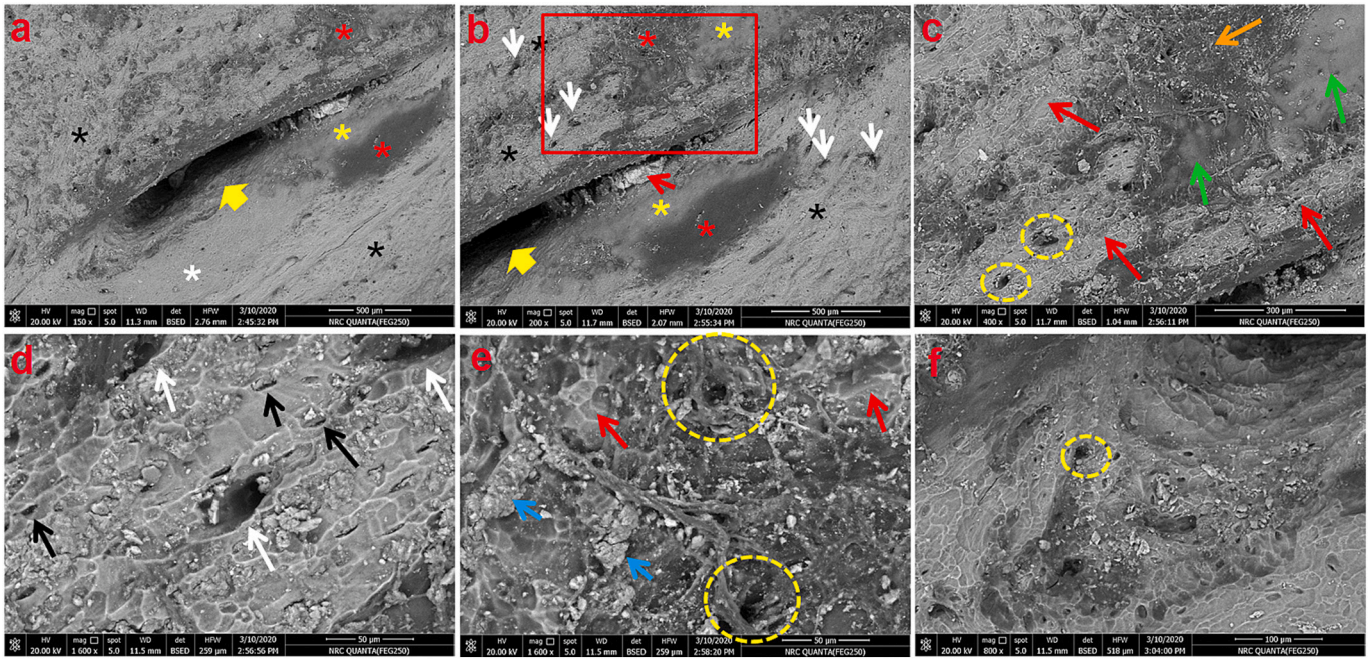

Fig. 13. (a-f) Shows SEM images taken for defect area at different magnification, the images are taken twenty weeks post-surgery.

of healing (20 weeks), the osteoid tissue (area donated by the yellow star) and collagenous organic matrix (areas donated by a red star) are limited and less noticed at the surface of the defect relative to the early stage of healing (10 weeks) as they mainly are transformed into mature bone. The area located within the red square seen in Fig. 13 (b) was further magnified in Fig. 13 (c). The magnified figure shows the progress of bone healing, where some mature bone fragments (indicated by red arrows) are seen penetrating and growing over the limited parts occupied by osteoid tissue (indicated by green arrows) and collagenous organic matrix (indicated by orange arrows). Furthermore, Haversian systems (located within yellow circles) are seen developed through the penetrated mature bone fragment indicating that active remodelling is

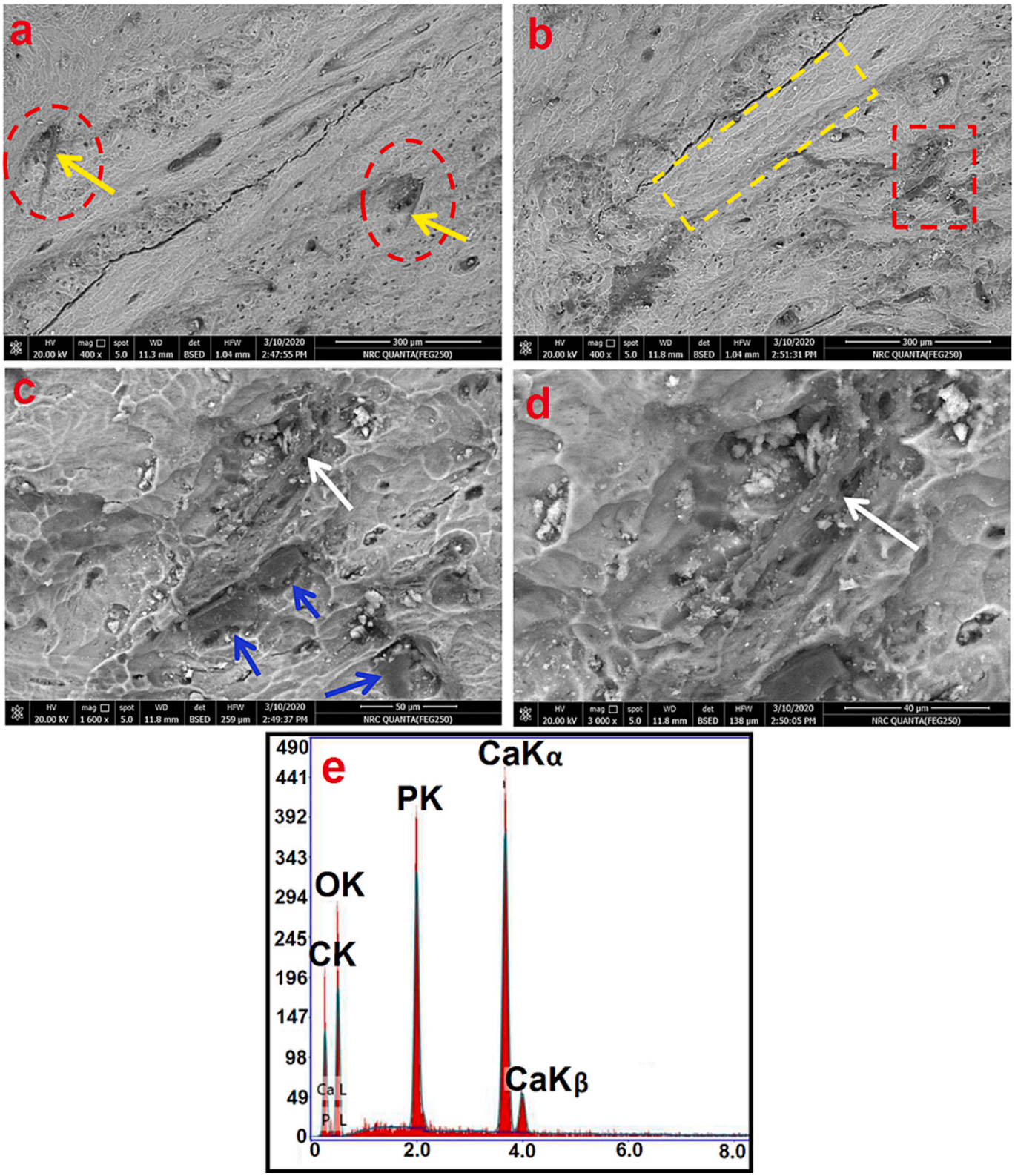

Fig. 14. (a-d) Shows different areas of developed bone at surface of the defect 20 weeks post-surgery (e) and EDX analysis of mature bone formed at the defect area.

being carried out as well. Fig. 13 (d) shows higher magnified views of Haversian systems (white arrows) and some osteocytes (black arrows) are seen located within their lacunae. The magnified view of the collagenous organic matrix is provided in Fig. 13 (e), where, several hydroxyapatite crystals are deposited on the matrix (blue arrow) or attached to collagen fibers. Also, small pieces of bone are seen grown on the organic matrix (red arrow). Some primary osteon structures are also created within the organic matrix (located within yellow circles). They can allow blood vessels to penetrate through the matrix to deliver oxygen and nourishment to cells. Finally, the innermost part of the defect area is indicated by yellow arrows in Fig. 13 (a) and (b), which were magnified in Fig. 13 (f) to evaluate the type of growing tissue within the defect. It is seen that both mature bone tissue and organic matrix are present. Yet, at this advanced stage of bone healing (20 weeks) the mineralized tissue is more expanded and occupied a larger space than at the early time point (10 weeks). Additionally, Haversian systems (surrounded by a yellow circle) are located through mineralized tissue inside the defect area indicating that active remodelling is taking place deep in the defect area beside bone remodelling at the surface of the defect.

Fig. 14 (a-d) shows different areas of developed bone at the surface of the defect 20 weeks post-surgery, which was filled with injectable hydrogel BP-B, where blood vessels (indicated by yellow arrows) are seen originating from well-developed Haversian systems (located within red circles). Fig. 13 (b) shows a few osteoclasts and one giant bone resorbing cell involved with active remodelling (located within the red square), also limited parts of formed bone are still immature bone (area enclosed within the yellow square). Figs. 14 (c) and (d) illustrate magnified views of osteoclasts (indicated by blue arrows) and one giant bone resorbing cell (denoted by white arrow) anchoring itself to the bone, where resorption pits and cavities are created. It is well-known that osteoclasts are responsible for removing excess mineralized bone tissue creating channels for the passage of blood vessels to deliver oxygen and food to cells [60]. EDX analysis of mature bone formed at the defect area 20 weeks post-surgery is provided in Fig. 14 (e). The analysis shows that Ca/P atomic ratio is 1.6 which is comparable to that of hydroxyapatite of normal bone.

SEM images for the defect areas of the control group showed that more bone was generated in the defect area 20 weeks post-surgery than that induce 10 weeks post-surgery as provided by Fig. 15 (a-e). Additionally, the defect border of the control group was well integrated with normal old bone at 20 weeks, and its margin was no longer separated or distinguished from surrounding old bone. Moreover, the developed bone became more mature at this higher time interval (20 weeks), and showed numerous Haversian systems (indicated by red arrows). Taking a closer look at the void area at the center of the defect, we can see parallel collagen fibers arranged at the side of the defect marked by black stars in Fig. 15 (b and c), besides small pieces of new bone are present as observed in Fig. 15 (b) (enclosed within the blue square). Moreover, few collagen fibers were trying to bridge the gap between the defect sides (pointed by the blue arrow) as noticed in Fig. 15 (b). The area inside the blue square is magnified in Fig. 15 (d and e), at which, a few pieces of growing bone are clearly noted (indicated by green arrows). EDX analysis of mature bone formed at the defect area of the control group 20 weeks post-surgery is provided in Fig. 15 (f). The analysis showed that Ca/P atomic ratio is 1.75, which is slightly higher than that of normal bone indicating that more bone remodelling is still needed to achieve the Ca/P atomic ratio of normal bone.

It was clearly observed that the amounts of formed new bone for the control group at both time intervals were less than that found in the defects area grafted with injectable hydrogel BP-B at the same time intervals. This provided evidence of the high capacity of injectable hydrogel BP-B for faster bone regeneration, remodelling and defect integration.

The natural healing process of long bone fractures is carried out through two main phases: endochondral bone formation, which is concerned with the production of the temporary cartilaginous matrix to provide stability for the defect area. This phase is carried out by chondrocytes as they can function properly under low oxygen conditions caused by the destruction of blood vessels in the defect area [61,62]. The second phase known as intramembranous ossification starts by recruiting osteoblasts and osteoclasts to the defect site through the newly developed blood vessels to laydown collagenous organic matrix and osteoid tissue to proceed with bone regeneration beside remodelling [61,62]. One remarkable feature of treating bone defects using a highly porous hydrogel is improving angiogenesis by allowing the newly developed blood vessels to penetrate from the surface of the implant towards its central part. Providing sufficient oxygen alongside nutrition to cells at an early stage of the restorative process is responsible for the

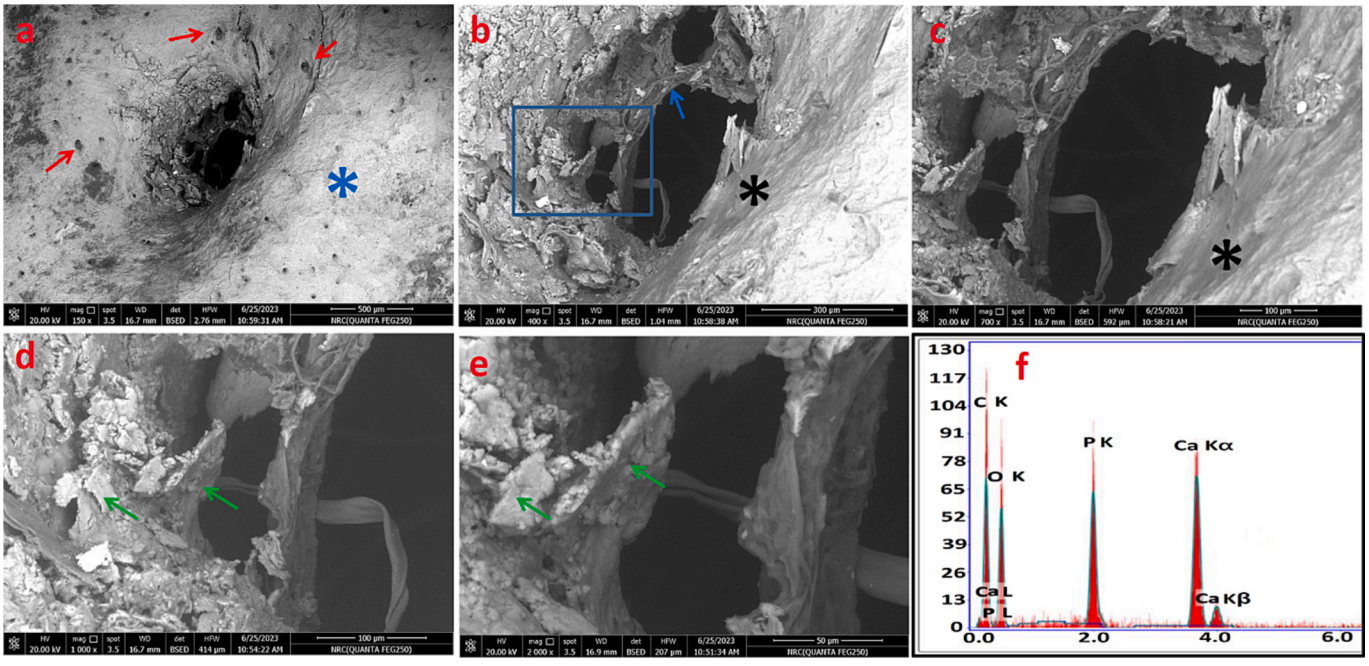

Fig. 15. (a-e) SEM images for the defect areas of the control group 20 weeks post-surgery.

completion of the endochondral ossification and bone healing sooner [26,63,64]. Additionally, using in-site gelling natural polymeric material such as alginate can replicate the native cartilaginous tissue secreted or induced by chondrocytes in the stage of endochondral ossification. Hence, these gelling materials can provide the stability to defect area and provide a matrix for chondrocytes to adhere, spread and start secreting collagen fibers. In return, it will control the duration time required for the termination of endochondral ossification, and accelerate the starting point of the osteogenesis stage. Overall, the progress of angiogenesis, endochondral ossification, and osteogenesis throughout the defect area will have a positive impact on reducing the healing time while ensuring the full restoration of well-mature bone tissue similar to the natural bone.

Also, hydroxyapatite nanoparticle (n-HA) has shown excellent osteoconductive, osteoinductive, oncogenic and immune-modulatory properties [26–28,65]. Immune-modulatory impact of n-HA is found to be responsible for directing the anti-inflammatory natural immune-mediated responses towards tissue repair and regeneration action [65]. These essential and indispensable properties of n-HA have an additional positive impact on speeding up the bone regeneration process observed herein. Moreover, natural polymers such as alginate include carboxylate groups which can initiate calcium precipitation and regulation of the in-situ bio-mineralization, which imitates the natural process of bone mineralization in the body [66,67]. On the other hand, the release of calcium and phosphorous ions from the hydroxyapatite nanoparticles included within the alginate gel improved and accelerated bone mineralization [26].

In vitro, bioactivity evaluation in simulated body fluid as in Fig. 6 has confirmed the ability of the Alg/n-HA sample to induce a well-mineralized hydroxyapatite layer on its surface. This layer is recognized and accepted by the bone cells as a part of normal bone inside the body. Thus, they become attached to the hydroxyapatite layer starting the bone formation alongside the remodelling process, and hence, it becomes transformed into fully mature bone [26–28]. Moreover, the induced hydroxyapatite layer on bioactive materials has a well-documented ability for protein adsorption (such as fibronectin) which are responsible for anchoring bone cells to the material surface [68]. An additional advantage of using an Alg/n-HA injectable hydrogel BP-B sample for bone healing is the presence of biogenic hydroxyapatite nanoparticles (n-HA) prepared from a natural source (eggshell). The used n-HA showed that it contains some trace elements in its composition [as in Table 2]. It is to be stated that the presence of trace elements such as manganese, cobalt, nickel, copper and chromium has a positive effect on bone regeneration and mineralization by stimulating angiogenesis at an early stage of bone healing [69 –73]. Copper-containing bioactive materials have shown beneficial biological activity by supporting cell adhesion, cell migration, chondrogenesis and osteogenesis, while at the same time providing unique antibacterial actions as well [74,75]. Additionally, it has a vital role in upregulating collagen production and cross-linking, which can affect bone matrix stability and strength [76]. The presence of strontium, gallium, zinc and lanthanum has also been documented in the n-HA. Those metals can induce the proliferation of bone marrow-derived mesenchymal stem cells and stimulate their osteogenic differentiation, which is essential for bone regeneration and mineralization [77–83]. In turn, bioactive materials incorporating one or more of these ions have shown the capacity to improve bone restoration and hasten defect healing [84–88]. They have shown the ability to reduce inflammation as well [89]. While the magnesium (Mg^{2+}) present in the n-HA will excellently immune-modulatory action via stimulating the transformation of macrophages from the M1 phase (pro-inflammatory induction phase) to the M2 phase (anti-inflammatory and tissue regenerative phase) [90–93]. This transformation at the defect site is highly vital for shifting the host response from inducing an acute inflammatory response (implant failure) towards a regenerative reaction by stimulating the osteogenic process leading to bone formation induction. M2 macrophages are responsible for provoking an immunomodulatory reaction that supports extracellular matrix production, bone remodelling and tissue healing [94]. The immune-modulatory response of magnesium is carried out by encouraging the production of different cytokines such as; anti-inflammatory (IL-10) and pro-osteogenic (TGF-β1 and BMP-2) cytokines, which are responsible for generating a more constructive osteoimmune microenvironment that effectively prompts the proliferation and differentiation of bone marrow mesenchymal stem cells towards osteogenic linkages [95]. Finally, the existence of SiO_2 as a modifier for the n-HA increased the bioactivity and ameliorated the capability for bone regeneration [96]. Therefore, the release of various vital and essential elements from implanted injectable hydrogel Alg/n-HA samples inside the defect area is probably responsible for its advanced bone healing properties documented in this work.

3.6. Histological evaluation

3.6.1. Ten weeks post-surgery injectable hydrogel BP-B and control group

Longitudinal histological sections (4 μ) were sliced deeply through the bone defect to evaluate the regeneration progress across the inner space or area within the defect 10 weeks after implantation injecting the Alg/n-HA hydrogel (BP —B sample), as provided in Fig. 16 (a-c) and (b). New bone (NB) is found surrounding the Alg/n-HA sample and on the material surface as well (indicated by a black arrow). Several osteocytes in lacunae were noticed (indicated by red arrows) distributed through the newly developed bone in Fig. 16 (a). Collagen fibers became highly organized around a central canal forming several primitive osteon structures as indicated by green arrows in Fig. 16 (a). The figure also shows multinucleated giant cells on the sample surface (denoted by blue arrows) besides numerous osteoblasts indicating the injectable hydrogel Alg/n-HA sample is not toxic to cells and revealing that active bone-forming/remodelling processes are taking place by these cells. The area enclosed within the blue square in Fig. 16 (a) was magnified in Fig. 16 (b). The magnified view showed a primitive osteon structure (located within a blue circle) that is surrounded by a few osteoblasts (blue arrow) is seen in the magnified view as well. It also shows some multinucleated giant cells (red arrow) involved in the active remodelling of newly developed bone tissue and material resorption. Fig. 16 (c) showed several osteoblasts (blue arrows) and osteoprogenitor cells (green arrows) scattering through the bone defect and on the material surface. They were engaged in secreting collagen fibers and extracellular bone matrix, which confirms that the active bone regeneration process is being carried out by cells through the defect area.

Longitudinal histological sections taken from the defect area of the control group 10 weeks post-surgery are provided in Fig. 17 (a and b). As

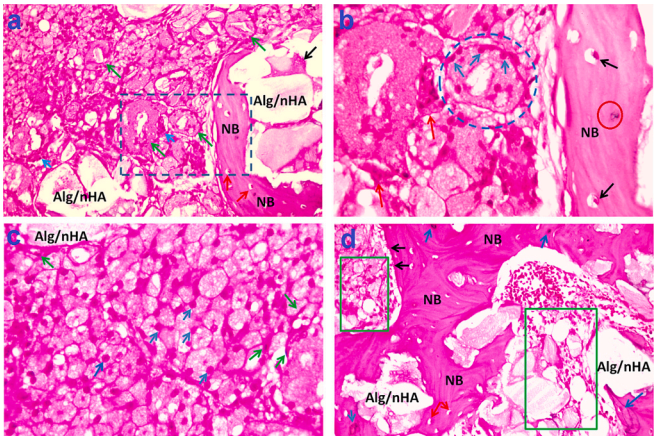

Fig. 16. Shows longitudinal histological sections taken from the internal part of bone defects grafted with Alg/n-HA injectable hydrogel (BP-B) at 10 weeks (a-c) and 20 weeks (b) post-surgery.

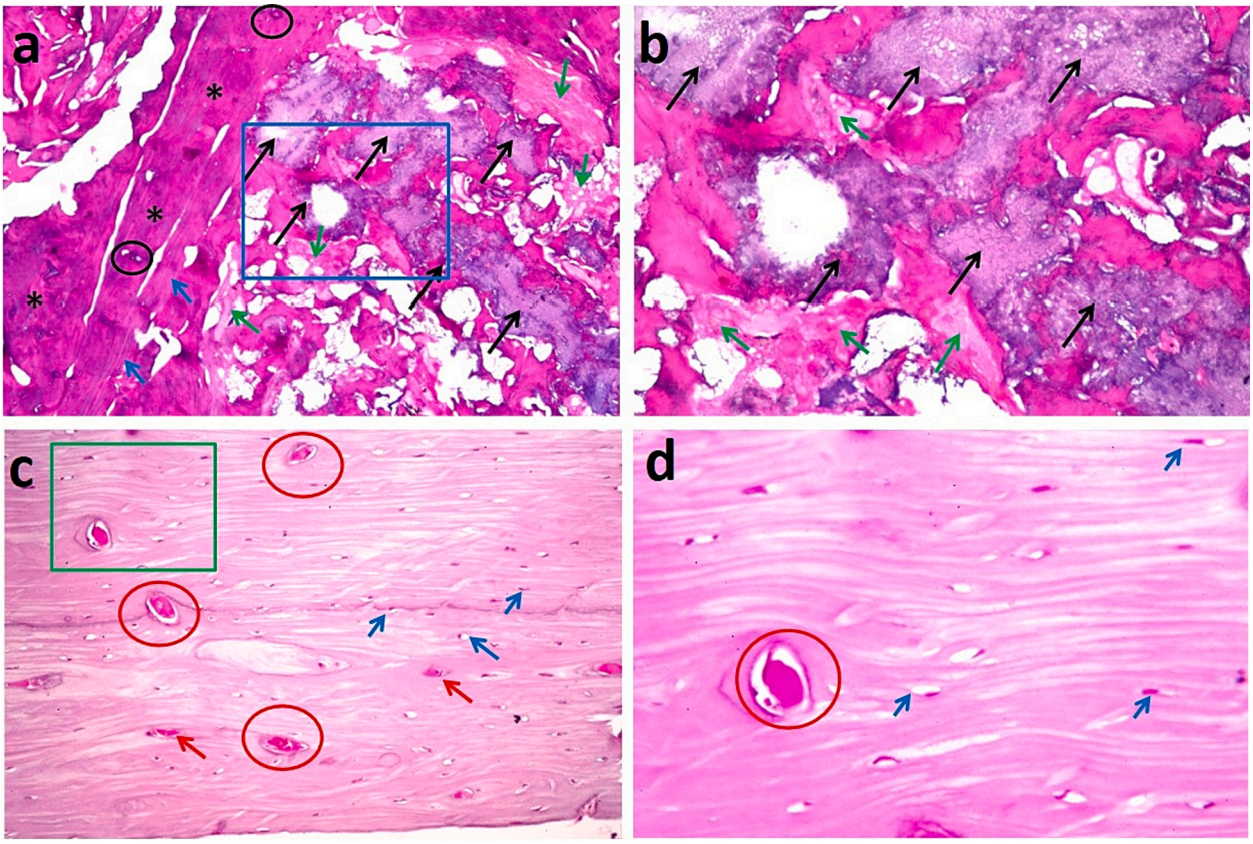

Fig. 17. Shows longitudinal histological sections taken from the internal part of bone defects grafted with Alg/n-HA injectable hydrogel (BP-B) at 10 weeks (a and b) and 20 weeks (c and d) post-surgery.

seen from the figure, new bone (donated by black stars) is formed near the border of the defect, where very few Haversian canals are noticed (marked by a black circle) in Fig. 17 (a). In addition, collagen fibers are organized beside the developed new bone (indicated by the blue arrow). In contrast, primitive cartilaginous tissues are found filling most of the central part of the defect area (pointed by black arrows) indicating that this part of the defect is still going through an early stage of endochondral bone formation. Moreover, fibrous connective tissue (indicated by the green arrow) is seen scattered in this central part as well. The area inside the blue square in Fig. 17 (a) is further magnified in Fig. 17 (b), where cartilaginous tissues is well observed (indicated by black arrows) and fibrous connective tissue is clearly noted.

3.6.2. *Twenty weeks post-surgery for injectable hydrogel BP-B and control group*

Fig. 16 (d) shows the longitudinal histological sections taken from the internal part of the bone defect grafted with injectable hydrogel Alg/n-HA, 20 weeks post-surgery. At this advanced stage, more space is shown to be occupied by the newly developed bone. Well-developed Haversian canals (blue arrows) are found distributed through new bone indicating that some parts of regenerated bone inside the defect area are transformed into mature bone. Still, some parts remain immature, which contained several osteocytes in lacunae (indicated by red arrows). Extensive spreading of bone cells is seen through the defect area and over the implanted samples (areas enclosed within green squares). New bone is grown on the surface of the sample as well. Additionally, red blood cells are seen on the sample indicating the passage of blood vessels through the implanted porous material, which can easily deliver oxygen and food to the cells. Some osteoclasts are seen engaged with the active remodelling at the border of the newly developed bone (denoted by black arrows) indicating that bone remodelling is continued through this advanced stage.

Longitudinal histological sections taken from the defect area of the control group 20 weeks post-surgery are seen in Fig. 17 (c and d). Several well-developed Haversian canals are noted (enclosed within red circles). No cartilage tissue was seen during this stage indicating that endochondral bone formation has ended and intramembranous bone formation is now in progress through this longer time interval (20 weeks). A large part of the defect is still osteoid tissue showing several osteocytes in lacunae (blue arrows). The area enclosed within a green square is magnified in Fig. 17(d). It is clearly seen that the upper parts of the defect are covered by parallel collagen fibers that are still not well interconnected.

Comparing between Alg/n-HA injectable hydrogel (BP —B sample) and control reveal that injectable hydrogel was able to accelerate both endochondral bone formation and intramembranous bone formation in defect area than the control group (defect was left empty).

3.7. *Bone mineral density measurements*

Bone mineral density (BMD) of the regenerated defect area grafted group with Alg/n-HA injectable hydrogel (BP —B sample) and control group was measured at 10- and 20 weeks post-surgery and results are represented in Fig. 18. The figure clearly shows that BMD increases with the duration of the grafting period both grafted group and control one. The measured BMD values for the defect area, grafted with Alg/n-HA injectable hydrogel (BP —B sample) at 10 and 20 weeks are 0.265 ± 0.05 and 0.344 ± 0.02, respectively. This increase in BMD is attributed to the improvement of bone maturation and mineralization with time. SEM examination of defect areas confirmed that less osteoid tissue and organic matrix existed at the advanced grafting stage (20 weeks) relative to the (10 weeks) stage. However, statistical analysis reveals that the difference in BMD values between two grafting time points is not significant ($p > 0.05$). This insignificant difference is attributed to the fact

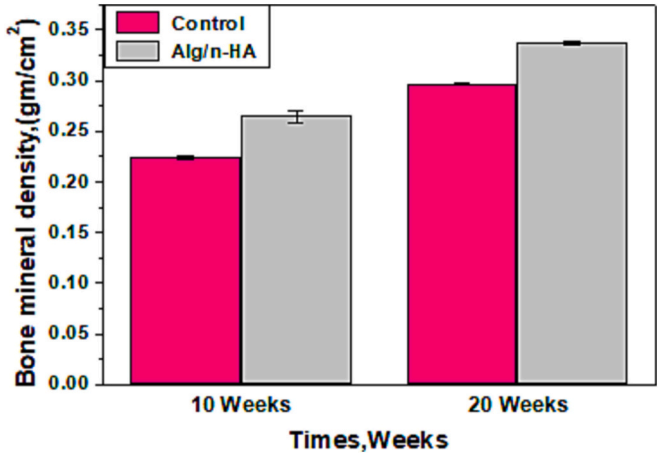

Fig. 18. Shows bone mineral density (BMD) of the regenerated defect area of grafted group with Alg/n-HA injectable hydrogel (BP —B sample) and control group measured at 10- and 20 weeks post-surgery.

that the bone maturation and/or mineralization process occurred during the early few weeks (10 weeks) and continued through the advanced stage of implantation (20 weeks). This fact is confirmed by SEM examination and histological evaluation. Both techniques have confirmed the presence of mature bone alongside immature bone in the defect area at the early grafting period. This mature bone becomes highly expanded through the defect area at the end of the advanced stage of grafting trials (20 weeks). For control group, the recorded BMD at 10 and 20 weeks are 0.224 ± 0.0135 and 0.297 ± 0.012, respectively. Comparing between BMD values of bone defects grafted with Alg/n-HA injectable hydrogel (BP —B sample) and those of control group indicated that grafted defects have higher values than defects of control group at both time interval. However, the difference is not significant at an early stage (10 weeks). This may be attributed to that both the grafted defects and empty holes of control group were able to regenerate sufficient amount of mature bone around defect margin at this early time interval. On the other hand, the difference between BMD values recorded for grafted defects with hydrogel and that of control group is found to be significant ($p = 0.046$) indicating that the generated bone in grafted defects is more mineralized and mature that that present in defects of control group at this higher time interval (20 weeks). These results proved the advantage of using injectable hydrogel for defect regeneration and augmentation, especially at higher time interval.

3.8. Radiology test

The radiographic image for the injectable hydrogel (BP-B) group after implantation for 10 weeks displayed a partially filled radiopacity. On the other hand, after 20 weeks of implantation, the radiopacity hole was almost full of newly formed bone (osteogenesis). So, it may be concluded that the injectable hydrogel (BP-B) group after implantation for 10 weeks possesses the highest radiolucency, tracked by the group implanted for 20 weeks displayed almost natural radio-opacity as in Fig. 19 (c-d).

Fig. 19 (a-b) shows an X-ray of rabbit femur bone specimens from the control group after 10 and 20 weeks of implantation in both anteroposterior and lateral views. The radiopacity only shows a radiolucent hole defect that does not extend to the compacta of the opposite side of the bone, indicating that bone formation is not entirely filling the marrow cavity.

3.9. Blood biochemistry studies

The following examinations were performed to estimate the implanted the health situation of the rabbits implanted for 10 and 20 weeks: liver and kidney functions, antioxidants profile, systemic inflammation, assessment for indicators of tumor progression, and hematology.

3.9.1. Liver function tests

It was noticed that the aspartate aminotransferase (ALT) level postoperative for the treated group injected with injectable hydrogel (BP-B) for 2.5–5 months was increased in comparison to the control group, Table 4. The ALT level increase is non-significant as the *p*-value equals 0.616. This increment is due to the rabbit's ageing during the experiment [97–99].

Furthermore, aspartate aminotransferase level (AST) for the group injected with injectable hydrogel (BP-B) for 2.5 and 5 months increased postoperative when compared to the control group, Table 4. But this increase is within the normal range as p value = 0.172, ($p > 0.05$), and the normal range of AST for rabbits is (10–98 IU/L). Alkaline phosphatase (ALP) is responsible for several vital functions and the increase in the activity of ALP refers to bone disease (ex, metastatic bone disease and fractures of bone). The ALP level of the treated group with injectable hydrogel (BP-B) for 2.5 months did not change on comparing with the control group. While ALP level was increased for the rabbits implanted for 5 months when compared to the control group. After 5 months the p-value was 0.122, which denoted the non-statically significance and the ALP value was in the normal range for healthy rabbits (10–96 IU/L), Table 4. The obtained results manifested the absence of unusual liver function results, which indicated that injection with Alg/n-HA injectable hydrogel (BP-B) did not cause fibrosis or injury of liver disease [99,100].

3.9.2. Kidney function tests

Creatinine level (Creat) of the rabbits implanted with injectable hydrogel BP-B for 2.5 and 5 months was decreased compared to that for the control rabbits' group, *P*-value is <0.05, which means that the difference is non-significant. While tracing the urea level in the rabbits grafted with injectable hydrogel BP-B for 2.5 and 5 months indicated a decrease when compared to the control rabbits' group. However, the variations were statistically not significant ($p > 0.05$). Total serum calcium (Ca^{2+}) shown in Table 3 displayed an increase during the short time of implantation (2.5 months), but it decreased after 5-month implantation. It is believed that the increase in the total Ca^{2+} level at the short time of implantation is due to the usage of a Ca cross-linker in addition to the saturation of the implant with Ca^{2+}. However, there is no significant difference ($p > 0.05$). Otherwise, the serum phosphorus (HPO_4^{-}) level was lower than that of the control group whether the implant was for 2.5 or 5 months and the statistical difference was not considerable $p > 0.05$. The kidney function results proved that the implantation of the injectable hydrogel (BP-B) for 2.5 or 5 months and the ions that were released did not cause a toxic effect on the kidney function, so the renal function is normal.

It is well known that phosphorus content in the blood influences the blood's calcium level. The increase in the calcium content led to a decrease in the phosphorous content [101]. Their existence in a balance keeps the bones well and powerful, while excess phosphorus withdraws the calcium from bones to preserve blood balance.

3.9.3. Antioxidants profile

It includes serum lipid hydroperoxide levels (LIP), serum glutathione reductase level (GSH), and superoxide dismutase (SOD).

The present study declared that GSH activity was slightly increased after 2.5 months of implantation of injectable hydrogel (BP-B) in the rabbits, while its value decreased after 5 months. The statistical difference is not considerable ($p > 0.05$), Table 4. The results are in agreement with Ragab et al., 2013 results [102]. On the other hand, the current results indicated that the LIP level for both implantation periods pointed out a decrease in LIP activity than that for the control group. Still the difference in un considerable statistically ($p > 0.05$), Table 4. The SOD level for the group injected for 2.5 months decreased compared to the

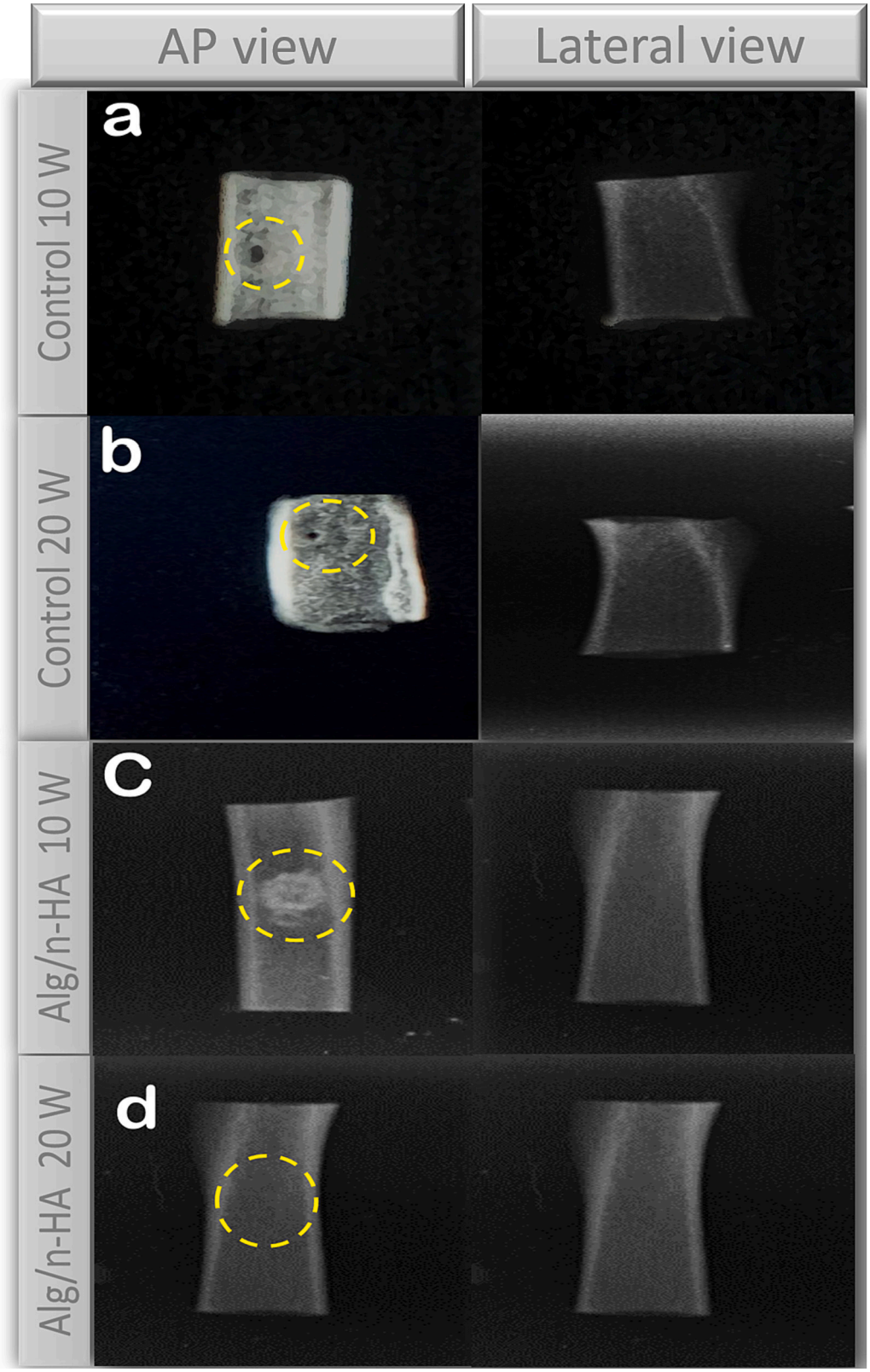

Fig. 19. Showing the radiographic (X-ray) picture in the femur bone of the rabbits for a) control group with hole defect after 10 weeks, b) control group after 20 weeks, c) group implanted with BP-B injectable hydrogel after 10 W, and d) group implanted with injectable hydrogel BP-B after 20 weeks for both Anteroposterior view, and lateral view.

Table 4
Shows the biochemistry results for rabbits injected with Alg/n-HA injectable hydrogel BP-B for 10- and 20-weeks post-surgery.

Test	Normal Range	Implantation time /Weeks					
		10			20		
		Control	Treated	Sig (ρ)	Control	Treated	Sig(ρ)
ALT (u/l)	55–260	24.80 ± 4.54	33.40 ± 0.75	0.01	37 ± 2.77	40.90 ± 2.31	0.62
AST (u/l)	10–98	42.40 ± 5.97	46.60 ± 3.9	0.64	50.80 ± 1.59	52.20 ± 1.87	0.17
ALP (Iu/l)	0–397	39.60 ± 2.58	39.90 ± 3.04	0.34	43.68 ± 0.95	50.50 ± 0.42	0.12
UREA (mg/dl)	13–30	30.60 ± 0.60	17.20 ± 0.49	0.02	28.00 ± 1.06	13.60 ± 2.46	0.07
CRAT (mg/dl)	0.5–2.6	1.12 ± 0.04	1.06 ± 0.10	0.14	0.94 ± 0.08	0.90 ± 0.07	0.89
Ca^{2+} (mg/dl)	5.5–12.5	10.78 ± 0.90	11.90 ± 0.50	0.09	11.82 ± 0.72	10.90 ± 0.29	0.82
P (mmol/l)	4–6	3.82 ± 0.71	2.74 ± 0.12	0.17	4.82 ± 0.34	2.98 ± 0.28	0.70
LIP (nmol/ml)	5–10.8	7.46 ± 0.70	5.40 ± 0.25	0.12	7.82 ± 0.73	4.20 ± 1.46	0.35
GSH (nmol/ml)	0.81–13.02	11.14 ± 0.66	13.10 ± 0.78	0.93	13.80 ± 0.58	10.40 ± 0.59	0.67
SOD (U/L)	0.1–28.5	3.06 ± 0.74	2.09 ± 0.43	0.52	2.98 ± 0.14	3.10 ± 0.21	0.53
NO (nmol/l)	3.12–19.36	6.83 ± 0.24	6.50 ± 0.23	0.87	8.28 ± 0.18	6.84 ± 0.17	0.75
ARG (ng/ml)	1.8–30	70.20 ± 5.38	63.40 ± 0.92	0.98	65.80 ± 0.86	60.00 ± 3.88	0.17
AFU (ng/ml)	0.6–8.5	3.300 ± 1.05	2.04 ± 0.254	0.146	5.60 ± 0.195	3.04 ± 0.802	0.21

control group. While the group injected for 5 months displayed increased SOD levels than the control group. The increment in the SOD level was not significant as the *p*-value =0.53. The obtained results agree with many authors [102,103].

3.9.4. Systemic inflammation (Nitric oxide, NO test)

This test is used to determine the degree of systemic inflammation from the grafted material injectable hydrogel (BP-B). The accumulation of the nitrite group is an indicator of nitric oxide production. The level of nitrite in the serum of the treated group for 2.5–5 months was lower than the control group. This decrease was not significant $p = 0.746$. The results agree with Naga et al., 2015 [104] and are in the rabbit's normal range [105].

3.9.5. Assessment for indicators of tumor progression

This profile includes both the arginase (ARG, u/ l) and ɑ-L-Fucosidase (AFU, u/ l) activities level in the serum of rabbits injected with injectable hydrogel (BP-B).

It was noticed that the ARG, u/ l activity level in the serum of injected rabbits was decreased than the control group for both injected periods, but the difference between injected animals and the control groups was not significant. On the other hand, the AFU level in the serum was lower than the control group for both injected periods as indicated in (Table 4). The difference between the AFU in the serum of the injected and control groups was insignificant. The obtained results proved that the degradation of injectable hydrogel (BP-B) has no oxidative influence and does not lead to the release of oxygen-free radicals that could destroy the living tissue, accordingly, the injectable Alg/n-HA injectable hydrogel is not a carcinogenic material.

3.9.6. Hematology test

The present study focused on the toxicity effect of injectable hydrogel (BP-B) on leukocyte count (WBCs), red blood cells (RBCs), hemoglobin levels (HB) and plate count (PLT) for the control and injected rabbits after 10- and 20-weeks post-operations. The results of Table 5 indicated that after 10 weeks the RBCs, WBCs and HA content were increased. Such an increase is due to the first step of natural healing, which names the defense mechanism of the living body against the implant. It is also noticed that the PTL count was decreased, but that reduction was within the normal range of rabbits' PTL count. Note: Values are expressed as a mean value ± standard deviation (SD) ($N = 5$). Significance level at $\rho<0.05$.

Table 6 represented the effect of injectable hydrogel (BP-B) on the WBCs, RBCs, HB and PLT counts for the control group and the group injected with injectable hydrogel (BP-B) 20 weeks post-operation. The results pointed out a decrease in the RBCs, WBCs, HB levels and PLT counts. The observed decrease is unnoticeable and the injected rabbits showed normal blood count levels. The results proved that injecting rabbits with Alg/n-HA did not poison or affect the health of the rabbits and that all hematology test results displayed normal results [104].

It is worth concluding that injection of injectable hydrogel (BP-B) in the femur of the rabbits has no toxic effect on the rabbits' health and that the complete healing of the bone injected area of the rabbits was faster than the control group. In addition, no side effects on pathological attitudes were noticed even after 20 weeks post operation.

4. Conclusion

We have successfully prepared and characterized bio-natural injectable hydrogels (Alg/n-HA composites) suitable for the replacement of irregular complicated bone shapes. The prepared injectable hydrogels can bone augmentations, they are utilizing pure nano-hydroxyapatite originating from eggshells, which was naturally enriched by suitable trace elements to mimic the composition of natural bones. The results displayed the following:

- Different injectable hydrogel samples, BP-1, BP-2, and BP-3, were produced by mixing a specific weight of nano-hydroxyapatite powder with 1, 2, and 4 ml of alginate solution.
- The physicomechanical properties examination revealed that the increase in the alginate solution content led to decreases in the

Table 5
The toxicity effect of injectable hydrogel BP-B implant on red blood cells (RBCs), white blood cells (WBCs), Hemoglobin level (HB) and platelet counts (PLT), 10 weeks post-operation.

Samples after 10 W	RBCs ($nx10^6$) N:(3.7–7.5) [106]	WBCs($nx10^3$) N: (5.20–16.5) [106]	HB g/dl N: (10–17.4) [106]	PLT ($nx10^3$) N: (112–795) [106]
Control	5.38 ± 0.25	13.12 ± 0.18	12.46 ± 0.16	188.00 ± 0.51
Alg/HA	5.78 ± 0.28	14.50 ± 0.15	12.82 ± 0.27	185.00 ± 0.64
SIG (ρ)	0.45	0.58	0.12	0.29

Table 6
The toxicity effect of injectable hydrogel BP-B injection on the red blood cells (RBCs), white blood cells (WBCs), Hemoglobin level (HB) and platelet counts (PLT), 20 weeks post-operation.

Samples After 20 W	RBCs ($nx10^6$) N: (3.7–7.5) [106]	WBCs($nx10^3$) N: (5.20–16.5) [106]	HB g/dl N: (10–17.4) [106]	PLT (nx103) N:(112–795) [106]
Control	7.38 ± 0.25	16.08 ± 0.11	16.68 ± 0.27	467.00 ± 7.90
Alg/HA	6.69 ± 0.25	15.22 ± 0.66	15.46 ± 0.17	439.00 ± 2.35
SIG (ρ)	0.72	0.07	0.16	0.36

compressive strength and increases in the setting time of injectable hydrogels.

- The results showed that the addition of polymeric gelling agents (Alg) cross-linked with $CaCl_2.2H_2O$ increased the net viscosity at the same temperature for all the prepared injectable pastes, and the injectable hydrogel (BP-B) is the suitable and easier one to handle.
- The weight loss of injectable hydrogel (BP-B) increased gradually from the 1st week to the 3rd week to reach 13.08 % of its initial weight during the incubation in PBS solution, notably lowering to 12.47 % by the end of the 4th week.
- The water absorption of the developed BP-B injectable hydrogel increased gradually from the 1st week of immersion to the 3rd week to reach 57.58 % of its initial weight, followed by a small decrease to 53.78 % in the 4th week.
- After 28 days of immersion in SBF, SEM examination revealed that the composite hydrogel's surface was completely covered with well-crystalline apatite particles with a Ca/P ratio of 1.65, a value that is close to the hydroxyapatite ratio. Such a result proved that the studied hydrogels possessed high bioactivity.
- In-vitro biochemical tests demonstrated no cytotoxicity effect.
- In-vivo study indicated that the presence of trace elements such as manganese, cobalt, nickel, copper and chromium have a positive effect on bone regeneration and mineralization by stimulating angiogenesis at an early stage of bone healing.
- Comparing between BMD values of bone defects grafted with Alg/n-HA injectable hydrogel (BP —B sample) and those of control group indicated that grafted defects has higher values than defects of control group at both time interval.
- It is to be stated that the injectable form of Alg/n-HA injectable hydrogel (BP-B) used as implant material was biocompatible, non-toxic and enhanced bone formation. It was detected histologically and ultra-structurally by the formation of osteoblasts, blood vessels, collagen and calcium crystals.

CRediT authorship contribution statement

Eman. M. Mahmoud: Conceptualization; Methodology (samples preparation and characterizations, in vivo tests); Formal analysis; Investigation; Data curation; Writing original draft. Mona Sayed: Conceptualization; Methodology (samples preparation and characterizations, in vitro tests); Formal analysis; Investigation; Data curation; Writing original draft. Abeer M El-Kady: Conceptualization; Methodology (in vivo tests); Formal analysis; Investigation; Data curation; histological, ultra structure results; Writing original draft. Samah. M. Kamel interpreting blood analysis, histological, ultra structure results. Salma M. Naga: Conceptualization; Supervision; Funding acquisition; Writing Review & Editing.

Declaration of competing interest

The authors declare that there is no conflict of interest.

Data availability

All data generated or analyzed during this study are included in this article.

Acknowledgements

This work was financed by the Science & Technology Development Fund (STDF), Egypt (German-Egyptian Research Fund (GERF) Projects program), Project ID 23036. Our thanks, and appreciation to the soul of the deceased Prof. Dr. Sayed El-Zomor Department of Surgery, Anesthesiology and Radiology, Faculty of Veterinary Medicine, Cairo University, Cairo, Egypt for his help in the X-ray analysis of rabbit's bones and the explanations of the radiology results.

References

[1] J.C. Reichert, S. Saifzadeh, M.E. Wullschleger, D.R. Epari, M.A. Schutz, G. N. Duda, H. Schell, M. van Griensven, H. Redl, D.W. Hutmacher, The challenge of establishing preclinical models for segmental bone defect research, Biomater. 30 (12) (2009) 2149–2163, https://doi.org/10.1016/j.biomaterials.2008.05.016.

[2] B.S. Jo, Y. Lee, J.S. Suh, Y.S. Park, H.J. Lee, J.Y. Lee, et al., A novel calcium-accumulating peptide/gelatin in situ forming hydrogel for enhanced bone regeneration, J. Bio. Med. Mater. Res. A 106 (2) (2018) 531–542, https://doi.org/10.1002/jbm.a.36257.

[3] N. Firouzi, A.B. Khoshfetrat, D. Kazemi, Enzymatically gellable gelatin improves nano-hydroxyapatite alginate microcapsule characteristics for modular bone tissue formation, J. Biomed. Mater. Res. 108A (2020) 340–350, https://doi.org/10.1002/jbm.a.36820.

[4] H. Samadian, H. Maleki, Z. Allahyari, M. Jaymand, Natural polymers-based light-induced hydrogels: promising biomaterials for biomedical applications, Coord. Chem. Rev. 420 (2020) 213432, https://doi.org/10.1016/j.ccr.2020.

[5] A.C. Hernández-González, L. Téllez-Jurado, L.M. Rodríguez-Lorenzo, Alginate hydrogels for bone tissue engineering, from injectables to bioprinting: a review, Carbohydr. Polym. 229 (2020) 115514, https://doi.org/10.1016/j.carbpol.2019.115514.

[6] H. Cassimjee, P. Kumar, Y.E. Choonara, V. Pillay, Proteosaccharide combinations for tissue engineering applications, Carbohydr. Polym. 235 (2020) 115932, https://doi.org/10.1016/j.carbpol.2020.115932.

[7] B. Taşdelen, S. Erdoğan, B. Bekar, Radiation synthesis and characterization of chitosan/hyraluronic acid/hydroxyapatite hydrogels: drug uptake and drug delivery systems, Mater. Today: Proceedings. 5 (2018) 15990–15997, https://doi.org/10.1016/j.matpr.2018.05.043.

[8] Y. Li, J. Rodrigues, H. Tomás, Injectable and biodegradable hydrogels: gelation, biodegradation and biomedical applications, Chem. Soc. Rev. 41 (2012) 2193–2221, https://doi.org/10.1039/c1cs15203c.

[9] Z. Zou, L. Wang, Z. Zhou, Q. Sun, D. Liu, Y. Chen, H. Hu, Y. Cai, S. Lin, Z. Yu, B. Tan, W. Guo, Z. Ling, X. Zou, Simultaneous incorporation of PTH (1–34) and nano-hydroxyapatite into chitosan/alginate hydrogels for efficient bone regeneration, Biomed. Mater. 6 (2021) 185–1839, https://doi.org/10.1016/j.bioactmat.2020.11.021.

[10] Z. Ning, B. Tan, B. Chen, D.S.A. Lau, T.M. Wong, T. Sun, et al., Precisely controlled delivery of abaloparatide through injectable hydrogel to promote bone regeneration, Macromol. Biosci. 19 (6) (2019) 1–9, https://doi.org/10.1002/mabi.201900020.

[11] R.A. Perez, J.H. Kim, J.O. Buitrago, I.B. Wall, H.W. Kim, Novel therapeutic core-shell hydrogel scaffolds with sequential delivery of cobalt and bone morphogenetic protein-2 for synergistic bone regeneration, Acta Biomater. 23 (2015) 295–308, https://doi.org/10.1016/j.actbio.2015.06.002.

[12] M.H. Nabavi, M. Salehi, A. Ehterami, F. Bastami, H. Semyari, M. Tehranchi, et al., A collagen-based hydrogel containing tacrolimus for bone tissue engineering, Drug Del. Transl. Res 10 (1) (2020) 108–121, https://doi.org/10.1007/s13346-019-00666-7.

[13] X. Fang, L. Lei, T. Jiang, Y. Chen, Y. Kang, Injectable thermosensitive alginate/beta-tricalcium phosphate/aspirin hydrogels for bone augmentation, J Biomed Mater Res B Appl Biomater 106 (5) (2018) 1739–1751, https://doi.org/10.1002/jbm.b.33982.

[14] A.S. Akay, V. Arisan, E. Cevher, M. Sessevmez, B. Cam, Oxytocin loaded sustained-release hydrogel graft provides accelerated bone formation: an experimental rat study, J. Orthop. Res. (2020) 1–12, https://doi.org/10.1002/jor.24607.

[15] L. Anqi, X. Huilin, Y. Peng, X. Jiaqi, D. Chunmei, Y. Xiaoqin, X. Jing, L. Jianshu, Injectable hydrogels based on gellan gum promotes *in situ* mineralization and potential osteogenesis, Eur. Polym. J. 141 (2020) 110091, https://doi.org/10.1016/j.eurpolymj.2020.110091.

[16] F. Asghari, M. Samiei, K. Adibkia, A. Akbarzadeh, S. Davaran, Biodegradable and biocompatible polymers for tissue engineering application: a review, Artif. Cells Nanomed. Biotechnol. 45 (2) (2017) 185–192, https://doi.org/10.3109/21691401.2016.1146731.

[17] L.S. Nair, C.T. Laurencin, Biodegradable polymers as biomaterials, Prog. Polym. Sci. 32 (8–9) (2007) 762–798, https://doi.org/10.1016/j.progpolymsci.2007.05.017.

[18] A. Tchobanian, H. Van Oosterwyck, P. Fardim, Polysaccharides for tissue engineering: current landscape and future prospects, Carbohydr. Polym. (2019) 601–625, https://doi.org/10.1016/j.carbpol.2018.10.039.

[19] J. Ying-Ying, Z. Ying-Jie, Li Heng, Z. Yong-Gang, S. Yue-Qin, S. Tuan-Wei, C. Feng, Preparation and enhanced mechanical properties of hybrid hydrogels comprising ultralong hydroxyapatite nanowires and sodium alginate, J. Colloid Interface Sci. 497 (2017) 266–275, https://doi.org/10.1016/j.jcis.2017.03.032.

[20] N. Hassan, Rasoul M. Sarraf, Dang Quang Svend Le, Cody Eric B, Fabrication of gelatin/hydroxyapatite/3D-graphene scaffolds by a hydrogel 3D-printing method, J. Mater. Chem. Phys. 239 (2020) 122305, https://doi.org/10.1016/j.matchemphys.2019.122305.

[21] R. Bowen, C. Xueyun, Du. Shoukang, Ma Ye, H. Chen, G. Yuan, Li Jianliang, D. Xiong, H. Tan, Li Zhonghua, Y. Chen, Hu Xiaohong, N. Xiaohong, Injectable polysaccharide hydrogel embedded with hydroxyapatite and calcium carbonate for drug delivery and bone tissue engineering, Int. J. Biol. Macromol. 118 (2018) 1257–1266, https://doi.org/10.1016/j.ijbiomac.2018.06.200.

[22] P. Wooram, S. Heejun, C. Bogyu, R. Won-Kyu, N. Kun, H. Dong Keun, Advanced hybrid nanomaterials for biomedical applications, Prog. Mater. Sci. 114 (2020) 100686, https://doi.org/10.1016/j.pmatsci.2020.100686.

[23] W. Cheng, Z. Ding, X. Zheng, Q. Lu, X. Kong, X. Zhou, G. Lu, L. David Kaplan, Injectable hydrogel systems with multiple biophysical and biochemical cues for bone regeneration, Aust. J. Biol. Sci. 8 (9) (2020) 2537–2548, https://doi.org/10.1039/d0bm00104j.
[24] Yon Jin C, Y. Peck, Jia En Josias Lau, H. Tak Hee, W. Dong-An, Hydrogel based cartilaginous tissue regeneration: recent insights and technologies, Aust. J. Biol. Sci. 28 (5 (4)) (2017) 613–631, https://doi.org/10.1039/c6bm00863a.
[25] Y.P. Singh, J.C. Moses, N. Bhardwaj, B.B. Mandal, Injectable hydrogels: a new paradigm for osteochondral tissue engineering, J. Mater. Chem. B 6 (2018) 5499, https://doi.org/10.1039/c8tb01430b.
[26] E.M. Mahmoud, M. Sayed, A.M. El-Kady, H. Elsayed, S.M. Naga, In vitro and in vivo study of naturally derived alginate/hydroxyapatite biocomposite scaffolds, Int. J. Biol. Macromol. 165 (2020) 1346–1360, https://doi.org/10.1016/j.ijbiomac.2020.10.014.
[27] S.M. Naga, E.M. Mahmoud, H.F. El-Maghraby, A.M. El-Kady, M.S. Arbid, A. Killinger, R. Gadow, Porous scaffolds based on biogenic poly (ε-caprolactone)/hydroxyapatite composites: in vivo study, Adv. Nat. Sci.: Nano Sci. Nanotechnol. 9 (045004) (2018) 12, https://doi.org/10.1088/2043-6254/aae9f7.
[28] S.M. Naga, E.M. Mahmoud, H.F. El-Maghraby, A.M. El-Kady, M.S. Arbid, A. Killinger, R. Gadow, Nano-biogenic hydroxyapatite porous scaffolds for bone regeneration, Interceram. Int. Ceram. Rev. 67 (2018) 36–42, https://doi.org/10.1007/s42411-018-0021-4.
[29] O.M. Clarkin, B. Wu, P.A. Cahill, D.F. Brougham, D. Banerjee, S.A. Brady, E. K. Fox, C. Lally, Novel injectable gallium-based self-setting glass-alginate hydrogel composite for cardiovascular tissue engineering, Carbohydr. Polym. 217 (2019) 152–159, https://doi.org/10.1016/j.carbpol.2019.04.016.
[30] A.M. El-kady, A.A. Ali, A. El-Fiqi, Controlled delivery of therapeutic ions and antibiotic drug of novel alginate-agarose matrix incorporating selenium-modified borosilicate glass designed for chronic wound healing, J. Non-Cryst. 534 (2020), 119889, https://doi.org/10.1016/j.jnoncrysol.2020.119889.
[31] P. Chuysinuan, P. Nooeaid, T. Thanyacharoen, S. Techasakul, P. Pavasant, K. Kanjanamekanant, Injectable eggshell-derived hydroxyapatite-incorporated fibroin-alginate composite hydrogel for bone tissue engineering, Int. J. Biol. Macromol. 193 (2021) 799–808, https://doi.org/10.1016/j.ijbiomac.2021.10.132.
[32] S.M. Naga, H.F. El-Maghraby, M. Sayed, E.A. Saad, Highly porous scaffolds made of nanosized hydroxyapatite powder synthesized from eggshells, J. Ceram. Sci. Technolo. 6 (3) (2015) 237–244, https://doi.org/10.4416/JCST2014-00058.
[33] I.W. Sutherland, in: David Byrom (Ed.), Biomaterials, Stockton Press, NY, 1991, p. 309.
[34] K. Ishikawa, Y. Miyamoto, M. Takechi, T. Toh, M. Kon, M. Nagayama, K. Asaoka, Tissue response to fast-setting calcium phosphate cement in bone, J. Biomed. Mater. Res. 37 (1997) 64–457, https://doi.org/10.1002/(sici)1097-4636(19971215)37:4<457, aid-jbm3>3.0.co;2-k.
[35] T. Kokubo, H. Takadama, How useful is SBF in predicting in vivo bone bioactivity? J. Biomater. 27 (15) (2006) 2907–2915, https://doi.org/10.1016/j.biomaterials.2006.01.017.
[36] S.K. Motwani, S. Chopra, S.K. Talegaonkar, et al., Chitosan-sodium alginate nanoparticles as submicroscopic reservoirs for ocular delivery: formulation, optimisation and in vitro characterisation, Eur. J. Pharm. Biopharm. 68 (3) (2008) 513–525, https://doi.org/10.1016/j.ejpb.2007.09.009.
[37] F.A. Macedo, E.H. Nunes, W.L. Vasconcelos, R.A. Santos, R.D. Sinisterra, M. E. Cortes, A biodegradable porous composite scaffold of PCL/BCP containing Ang- (1–7) for bone tissue engineering, Ceràm 58 (348) (2012) 481–488, https://doi.org/10.1590/S0366-69132012000400011.
[38] ASTM C-20; Standard Test Methods for Apparent Porosity, Water Absorption, Apparent Specific Gravity, and Bulk Density of Burned Refractory Brick and Shapes by Boiling Water n.d.
[39] DIN EN ISO 6872, Dental Ceramic (ISO 6872:1995 including amendment 1: 1997); English version of DIN EN ISO 6872, 1999.
[40] International Standards ISO 9917–-1, Reference number Iso 9917–1:2003 (E) Dentistry-Water-Based cements-part 1: powder/liquid acid-base cements, 2003. E.
[41] M. Litwin, H. Tan, The diagnosis and treatment of prostate cancer: a review, JAMA 317 (24) (2017) 2532–2542, https://doi.org/10.1001/jama.2017.7248.
[42] J. Banchroft, A. Stevens, D.R. Turner, Theory and Practice of Histological Techniques, Fourth Ed, Churchil Livingstone, New York, London, San Francisco, Tokyo, 1996.
[43] J. Elliott, Structure and Chemistry of the Apatites and Other Calcium Orthophosphates, Elsevier Science, Amsterdam, 1994.
[44] W. Xue, Aug, et al., Osteoprecursor cell response to strontium-containing hydroxyapatite ceramics, J. Biomed. Mater. Res. 79A (4) (2006) 804–814, https://doi.org/10.1002/jbm.a.30815.
[45] C. Capuccini, P. Torricelli, E. Boanini, M. Gazzano, R. Giardino, A. Bigi, Interaction of Sr-doped hydroxyapatite nanocrystals with osteoclast and osteoblastlike cells, J. Biomed. Mater. Res. 89A (3) (2009) 594–600, https://doi.org/10.1002/jbm.a.31975.
[46] N. Neves, D. Linhares, G. Costa, C.C. Ribeiro, M.A. Barbosa, In vivo and clinical application of strontium-enriched biomaterials for bone regeneration: a systematic review, Bone Jt. Res. 6 (6) (2017) 366–375, https://doi.org/10.1302/2046-3758.66.BJR-2016-0311.R1.
[47] R. Marsell, T.A. Einhorn, The biology of fracture healing, J. Injury. 42 (6) (2011) 551–555, https://doi.org/10.1016/j.injury.2011.03.031.
[48] K.B. Headley, S.M. Newman, J.R. Hunt, Dietary zinc reduces osteoclast resorption activities and increases markers of osteoblast differentiation, matrix maturation, and mineralization in the long bones of growing rats, J. Nutra. Biol. chem. 21 (2010) 297–303, https://doi.org/10.1016/j.jnutbio.2009.01.002.
[49] I. Zofkova, M. Davis, J. Blahos, Trace elements have beneficial, as well as detrimental effects on bone homeostasis, Physiol. Res. 66 (2017) 391–402, https://doi.org/10.33549/physiolres.933454.
[50] S. Xu, Q. Wu, B. He, J. Rao, D.H.K. Chow, J. Xu, X. Wang, Y. Sun, C. Ning, K. Dai, Interactive effects of cerium and copper to tune the microstructure of silicocarnotite bioceramics towards enhanced bioactivity and good biosafety, Biomater. 288 (2022) 121751, https://doi.org/10.1016/j.biomaterials.2022.121751.
[51] N. Eliaz, N. Metoki, Calcium phosphate bioceramics: a review of their history, structure, properties, coating technologies and biomedical applications, Mater. 334 (10) (2017) 1–104, https://doi.org/10.3390/ma10040334.
[52] S.V. Dorozhkin, Calcium orthophosphate cements and concretes, Mater. 2 (2009) 221–291, https://doi.org/10.3390/ma2010221.
[53] S.T. Bendtsen, S.P. Quinnell, M. Wei, Development of a novel alginate-polyvinyl alcohol-hydroxyapatite hydrogel for 3D bioprinting bone tissue engineered scaffolds, J. Biomed. Mater. Res. Part A (105(5)) (2017) 1457–1468, https://doi.org/10.1002/jbm.a.360.
[54] P. Hui, S.L. Meena, G. Singh, R.D. Agarawal, S. Prakashe, Synthesis of hydroxyapatite bio-ceramic powder by hydrothermal method, JMMCE. 9 (8) (2010) 683–692, https://doi.org/10.4236/jmmce.2010.98049.
[55] G. Gergely, F. Wéber, I. Lukács, L. Illés, A.L. Tóth, Z.E. Horváth, J. Mihály, C. Balázsi, Nano-hydroxyapatite preparation from biogenic raw materials, Cent. Eur. J. Chem. 8 (2) (2010) 375–381, https://doi.org/10.2478/s11532-010-0004-4.
[56] Y.C. Huang, P.C. Hsiao, H.J. Chai, Hydroxyapatite extracted from fish scale: effects on MG63 osteoblast-like cells, Ceram. Int. 37 (2011) 1825–1831, https://doi.org/10.1016/j.ceramint.2011.01.018.
[57] T. Chae, H. Yang, V. Leung, F. Ko, T. Troczynski, Novel biomimetic hydroxyapatite/alginate nanocomposite fibrous scaffolds for bone tissue regeneration, J. Mater. Sci. Mater. Med. 24 (2013) 1885–1894, https://doi.org/10.1007/s10856-013-4975-7.
[58] H.S. Kim, S.G. Kumbar, S.P. Nukavarapu, Amorphous silica fiber matrix biomaterials: an analysis of material synthesis and characterization for tissue engineering, Bioact. Mater. 19 (2023) 155–166, https://doi.org/10.1016/j.bioactmat.2022.04.002.
[59] G.T. Grant, E.R. Morris, D.A. Rees, P.J. Smith, D. Thom, Biological interaction between polysaccharides and di-valent cations: the egg-box model, FEBS Lett. 32 (1973) 195–198, https://doi.org/10.1016/0014-5793(73)80770-7.
[60] S. Boonrungsiman, E. Gentleman, R. Carzaniga, et al., The role of intracellular calcium phosphate in osteoblast-mediated bone apatite formation, PNAS. 109 (35) (2012) 14170–14175, https://doi.org/10.1073/pnas.1208916109.
[61] A. Bigham-Sadegh, A. Oryan, Basic concepts regarding fracture healing and the current options and future directions in managing bone fractures, Int. Wound J. 12 (2014) 238–247, https://doi.org/10.1111/iwj.12231.lISSN1742-4801.
[62] J. Webb, J. Tricker, Bone biology a review of fracture healing, J. Curr. Orthopaed. 14 (2000) 457–463, https://doi.org/10.1054/cuor.2000.0145.
[63] E.J. Sheehy, D.J. Kelly, F.J. O'Brien, Biomaterial-based endochondral bone regeneration: a shift from traditional tissue engineering paradigms to developmentally inspired strategies, Mater. Today Bio. 3 (2019) 1–13, https://doi.org/10.1016/j.mtbio.2019.100009.
[64] M.I. Santos, R.L. Reis, Vascularization in bone tissue engineering: physiology, current strategies, major hurdles and future challenges, Macromol. Biosci. 10 (1) (2010) 12–27, https://doi.org/10.1002/mabi.200900107.
[65] M. Joanna Sadowska, M. Ginebra, Inflammation and biomaterials: role of the immune response in bone regeneration by inorganic scaffolds, J. Mater. Chem. B 8 (2020) 9404, https://doi.org/10.1039/d0tb01379j.
[66] J. Ming, Z. Jiang, P. Wang, S. Bie, B. Zuo, Silk fibroin/sodium alginate fibrous hydrogels regulated hydroxyapatite crystal growth, Mater. Sci. Eng. C 51 (2015) 287–293, https://doi.org/10.1016/j.msec.2015.03.014.
[67] L. Addadi, S. Weiner, Interactions between acidic proteins and crystals: stereochemical requirements in biomineralization, PNAS. 82 (1985) 4110–4114, https://doi.org/10.1073/pnas.82.12.4110.
[68] L.L. Hench, Bioceramics, J. Am. Ceram. Soc. 81 (1998) 1705–1728, https://doi.org/10.1111/j.1151-2916.1998.tb02540.x.
[69] S. Kulanthaivel, B. Roy, T. Agarwal, S. Giri, K. Pramanik, K. Pal, S.S. Ray, T. K. Maiti, I. Banerjee, Cobalt doped proangiogenic hydroxyapatite for bone tissue engineering application, Mater. Sci. Eng. C 58 (2016) 648–658, https://doi.org/10.1016/j.msec.2015.08.052.
[70] Z. Deng, B. Lin, Z. Jiang, W. Huang, J. Li, X. Zeng, H. Wang, D. Wang, Y. Zhang, Hypoxia-mimicking cobalt-doped borosilicate bioactive glass scaffolds with enhanced angiogenic and osteogenic capacity for bone regeneration, Int. J. Biol. Sci. 15 (2019) 1113–1124, https://doi.org/10.7150/ijbs.32358.
[71] C. Wu, Y. Zhou, M. Xu, P. Han, L. Chen, J. Chang, Y. Xiao, Copper containing mesoporous bioactive glass scaffolds with multifunctional properties of angiogenesis capacity, osteostimulation and antibacterial activity, Biomater. 34 (2013) 422–433, https://doi.org/10.1016/j.biomaterials.2012.09.066.
[72] M.A. Saghiri, A. Asatourian, J. Orangi, M. Christine Sorenson, N. Sheibani, Functional role of inorganic trace elements in angiogenesis—Part II: Cr, Si, Zn, Cu, and S, Crit. Rev. Oncol./Hematol. 96 (2015) 15–143, https://doi.org/10.1016/j.critrevonc.2015.05.011.
[73] S. Haque, S. Tripathy, C. Ranjan Patra, Manganese-based advanced nanoparticles for biomedical applications: future opportunity and challenges, Nanoscale. 13 (2021) 16405–16426, https://doi.org/10.1039/d1nr04964j.

[74] Y. Wang, W. Zhang, Q. Yao, Copper-based biomaterials for bone and cartilage tissue engineering, Journal of Orthopaedic Translation 29 (2021) 60–71, https://doi.org/10.1016/j.jot.2021.03.003.
[75] J.M. Cordeiro, V.A.R. Barão, E.D. de Avila, J.F.A. Husch, F. Yang, J.J.P. Jeroen van den Beucken, Tailoring Cu^{2+} loaded electrospun membranes with antibacterial ability for guided bone regeneration, Biomater. Adv. 139 (2022), 212976, https://doi.org/10.1016/j.bioadv.2022.212976.
[76] C. Yue, C. Dinga, J. Sua, B. Chenga, Effect of copper and zinc ions on type I collagen self-assembly, Int. J. Polym. Anal. Charact. 27 (6) (2022) 394–408, https://doi.org/10.1080/1023666X.2022.2093569.
[77] T. Lu, X. Yuan, L. Zhang, F. He, X. Wang, Y. Zhang, J. Ye, High through put synthesis and screening of zinc-doped biphasic calcium phosphate for bone regeneration, Appl. Mater. Today 25 (2021) 101225, https://doi.org/10.1016/j.apmt.2021.101225.
[78] F. He, C. Qiu, Y. Wang, T. Lu, J. Ye, Synthesis, characterization and cell response of silicon/gallium co-substituted tricalcium phosphate bioceramics, J. Mater. Sci. 57 (2022) 1302–1313, https://doi.org/10.1007/s10853-021-06584-9.
[79] C. Qiu, T. Lu, F. He, S. Feng, X. Fang, F. Zuo, Q. Jiang, X. Deng, J. Ye, Influences of gallium substitution on the phase stability, mechanical strength and cellular response of β-tricalcium phosphate bioceramics, Ceram. Int. 46 (2020) 16364–16371, https://doi.org/10.1016/j.ceramint.2020.03.195.
[80] V.M. Schatkoski, T.L. do Amaral Montanheiro, B.R.C. de Menezes, R.M. Pereira, K.F. Rodrigues, R.G. Ribas, D.M. da Silva, G.P. Thim, Current advances concerning the most cited metal ions doped bioceramics and silicate-based bioactive glasses for bone tissue engineering, Ceram. Int. 47 (2021) 301–2999, https://doi.org/10.1016/j.ceramint.2020.09.213.
[81] N.H. Lee, M.S. Kang, T.H. Kim, D.S. Yoon, N. Mandakhbayar, S.B. Jo, H.S. Kim, J. C. Knowles, J.H. Lee, H.W. Kim, Dual actions of osteoclastic-inhibition and osteogenic stimulation through strontium-releasing bioactive nanoscale cement imply biomaterial enabled osteoporosis therapy, Biomater. 276 (2021) 121025, https://doi.org/10.1016/j.biomaterials.2021.121025.
[82] Z. Xu, B. Lin, C. Zhao, Y. Lu, T. Huang, Y. Chen, J. Li, R. Wu, Wenge Liu, J. Lin, Lanthanum doped octacalcium phosphate/polylactic acid scaffold fabricated by 3D printing for bone tissue engineering, J. Mater. Sci. Technol. 118 (2022) 229–242, https://doi.org/10.1016/j.jmst.2021.09.069.
[83] R. Guo, X. Hou, D. Zhao, H. Wang, C. Shi, Y. Zhou, Mechanical stability and biological activity of mg–Sr co-doped bioactive glass/chitosan composite scaffolds, J. Non-Cryst. Solids 583 (2022) 121481, https://doi.org/10.1016/j.jnoncrysol.2022.121481.
[84] X. Bai, W. Liu, L. Xu, Q. Ye, H. Zhou, C. Berg, H. Yuan, J. Li, W. Xia, Sequential macrophage transition facilitates endogenous bone regeneration induced by Zn-doped porous microcrystalline bioactive glass, J. Mater. Chem. B 9 (2021) 2885, https://doi.org/10.1039/d0tb02884c.
[85] Z. Zhong, X. Wu, Y. Wang, M. Li, Y. Li, X. Liu, X. Zhang, Z. Lan, J. Wang, Yi Du, S. Zhang, Zn/Sr dual ions-collagen co-assembly hydroxyapatite enhances bone regeneration through procedural osteo-immunomodulation and osteogenesis, Bioact. Mater. 10 (2022) 195–206, https://doi.org/10.1016/j.bioactmat.2021.09.013.
[86] F. Kurtuldu, N. Mutlu, A.R. Boccaccini, D. Galusek, Gallium containing bioactive materials: a review of anticancer, antibacterial, and osteogenic properties, Bioact. Mater. 17 (2022) 125–146, https://doi.org/10.1016/j.bioactmat.2021.12.034.
[87] M. Vukomanovic, L. Gazvoda, N. Anicic, M. Rubert, D. Suvorov, R. Müller, S. Hofmann, Multi-doped apatite: strontium, magnesium, gallium and zinc ions synergistically affect osteogenic stimulation in human mesenchymal cells important for bone tissue engineering, Biomater. Adv. 140 (2022) 213051, https://doi.org/10.1016/j.bioadv.2022.213051.
[88] S. Wang, R. Gu, F. Wang, X. Zhao, F. Yang, Y. Xu, F. Yan, Y. Zhu, D. Xia, Yunsong Liu, 3D-Printed PCL/Zn scaffolds for bone regeneration with a dose-dependent effect on osteogenesis and osteoclastogenesis, Mater Today Bio. 13 (2022), 100202, https://doi.org/10.1016/j.mtbio.2021.100202.
[89] H. Agarwal, A. Nakara, V.K. Shanmugam, Anti-inflammatory mechanism of various metal and metal oxide nanoparticles synthesized using plant extracts: a review, Biomed. Pharmacother. 109 (2019) 2561–2572, https://doi.org/10.1016/j.biopha.2018.11.116.
[90] H. Zhoua, B. Liang, H. Jiang, Z. Deng, K. Yu, Magnesium-based biomaterials as emerging agents for bone repair and regeneration: from mechanism to application, JMA 9 (2021) 779–804, https://doi.org/10.1016/J.JMA.2021.03.004.
[91] M. Wang, Y. Yu, K. Dai, Z. Ma, Y. Liu, J. Wang, C Liu, improved osteogenesis and angiogenesis of magnesium-doped calcium phosphate cement *via* macrophage immunomodulation, Biomater Sci. 4 (2016) 1574–1583, https://doi.org/10.1039/c6bm00290k.
[92] D. Qi, J. Su, S. Li, H. Zhu, Lijin Cheng, S. Hua, Xi Yuan, Jiawei Jiang, Zixing Shu, Y. Shi, J. Xiao, 3D printed magnesium-doped β-TCP gyroid scaffold with osteogenesis, angiogenesis, immunomodulation properties and bone regeneration capability in vivo, Biomater. Adv. 136 (2022), 212759, https://doi.org/10.1016/j.bioadv.2022.212759.
[93] B. Chen, Z. Lin, Q. Saiding, Y. Huang, Y. Sun, X. Zhai, Z. Ning, H. Liang, W. Qiao, B. Yu, K.W.K. Yeung, J. Shen, Enhancement of critical-sized bone defect regeneration by magnesium oxide-reinforced 3D scaffold with improved osteogenic and angiogenic properties, J. Mater. Sci. Technol. 135 (2023) 186–198, https://doi.org/10.1016/j.jmst.2022.06.036.
[94] Y. Niu, Z. Wang, Y. Shi, L. Dong, C. Wang, Modulating macrophage activities to promote endogenous bone regeneration: biological mechanisms and engineering approaches, Bioact. Mater. 6 (2020) 244–261, https://doi.org/10.1016/j.bioactmat.2020.08.012.
[95] Y. Peng, J. Yang, W. Fu, Q. Gao, S. Yao, C. Peng, S. Hou, Osteoimmunomodulatory properties of a magnesium-doped phase-transited lysozyme coating on titanium, Mater.Today. Adv. 14 (2022) 100234, https://doi.org/10.1016/j.mtadv.2022.100234.
[96] X. Yuan, Y. Xu, T. Lu, F. H, L. Zhang, Q. He, J. Ye, Enhancing the bioactivity of hydroxyapatite bioceramic via encapsulating with silica-based bioactive glass sol, J. Mech. Behav. Biomed. Mater. 128 (2022), 105104, https://doi.org/10.1016/j.jmbbm.2022.105104.
[97] A. Jenner, M. Ren, R. Rajendran, P. Ning, B.T. Huat, F. Watt, B. Halliwell, Zinc upplementation inhibits lipid peroxidation and the development of atherosclerosis in rabbits fed a high cholesterol diet, Free Radic. Biol. Med. 42 (4) (2007) 559–566, https://doi.org/10.1016/j.freeradbiomed.2006.11.024.
[98] A. Hatipoglu, O. Kanbagli, J. Balkan, M. Kucuk, U. Cevikbas, G. Aykac Toker, H. Berkkan, M. Uysal, Hazelnut oil administration reduces aortic cholesterol accumulation and lipid peroxides in the plasma, liver, and aorta of rabbits fed a high- cholesterol diet, Biosci. Biotechnol. Biochem. 68 (10) (2004) 57–2050, https://doi.org/10.1271/bbb.68.2050.
[99] P.N. Newsome, R. Cramb, S.M. Davison, J.F. Dillon, M. Foulerton, E.M. Godfrey, R. Hall, U. Harrower, M. Hudson, A. Langford, A. Mackie, R. Mitchell-Thain, K. Sennett, N.C. Sheron, J. Verne, M. Walmsley, A. Yeoman, Guidelines on the management of abnormal liver blood tests, Gut 67 (1) (2018) 6–19, https://doi.org/10.1136/gutjnl-2017-314924.
[100] M.D. Mahbubur Rahman, Hematology and Biochemistry of New Zealand White Rabbits 24, 2018, pp. 1–51, https://doi.org/10.13140/RG.2.2.11903.05287/1.
[101] F.T. Fischbach, M.B. Dunning III (Eds.), Manual of Laboratory and Diagnostic Tests, 8th ed., Lippincott Williams and Wilkins, Philadelphia, 2009.
[102] A.R. Ragab, M.A. Elkablawy, B.Y. Sheik, H.N. Baraka, Antioxidant and tissue protective studies on ajwa extract: Dates from Al Madinah Al-Monwarah, Saudi Arabia, J. Environ. Anal. Toxicol. 3 (1) (2013) 1–8, https://doi.org/10.4172/2161-0525.1000163.
[103] L.S. Lee, C.W. Cho, H.D. Hong, Y.C. Lee, U.K. Choi, Y.C. Kim, Hypolipidemic and antioxidant properties of phenolic compound-rich extracts from white ginseng (Panax ginseng) in cholesterol-fed rabbits, Mol. 18 (10) (2013) 60–12548, https://doi.org/10.3390/molecules181012548.
[104] S.M. Naga, M.M.S. Wahsh, A.M. El-Kady, H.I.E. Asaker, Synthesis, in vitro and in vivo behaviour of TiO2 containing inorganic/organic hybrids, Interceram 64 (4) (2015) 292–297, https://doi.org/10.1007/BF03401136.
[105] C. Ozkan, A. Kaya, Y. Akgül, Normal values of hematological and some biochemical parameters in serum and urine of New Zealand white rabbits, World Rabbit Sci. 20 (4) (2012) 253–259, https://doi.org/10.4995/wrs.2012.1229.
[106] C.D. Hewitt, D.J. Innes, J. Savory, M.R. Wills, Normal biochemical and hematological values in New Zealand white rabbits, Clin. Chem. 35 (8) (1989) 1777–1779, https://doi.org/10.1093/clinchem/35.8.1777.